

Objective frequentist uncertainty quantification for atmospheric CO₂ retrievals*

Pratik Patil[†], Mikael Kuusela[‡], and Jonathan Hobbs[§]

Abstract. The steadily increasing amount of atmospheric carbon dioxide (CO₂) is affecting the global climate system and threatening the long-term sustainability of Earth’s ecosystem. In order to better understand the sources and sinks of CO₂, NASA operates the Orbiting Carbon Observatory-2 & 3 satellites to monitor CO₂ from space. These satellites make passive radiance measurements of the sunlight reflected off the Earth’s surface in different spectral bands, which are then inverted to obtain estimates of the atmospheric CO₂ concentration. In this work, we first analyze the current operational retrieval procedure, which uses prior knowledge in the form of probability distributions on the relevant atmospheric state variables to regularize the underlying ill-posed inverse problem, and demonstrate that the resulting uncertainties might be poorly calibrated both at individual locations and over a spatial region. To alleviate these issues, we propose a new method that uses known physical constraints on the state variables and direct inversion of the target functionals of the CO₂ profile to construct well-calibrated frequentist confidence intervals based on convex programming. Furthermore, we study the influence of individual nuisance state variables on the length of the confidence intervals and identify certain key variables that can greatly reduce the final uncertainty given additional deterministic or probabilistic constraints, and develop a principled framework to incorporate such information into our method.

Key words. Orbiting Carbon Observatory-2 & 3, remote sensing, constrained inverse problem, frequentist coverage, variable importance, convex programming

AMS subject classifications. 62P12, 15A29, 62F30, 90C90

1. Introduction. Global measurements of atmospheric carbon dioxide (CO₂) concentration are essential for understanding Earth’s carbon cycle, a key component of our planet’s climate system. Space-borne observing systems provide the primary way of obtaining atmospheric CO₂ measurements globally at spatial and temporal resolutions useful for investigating central questions in carbon cycle science [32]. A series of satellites named Orbiting Carbon Observatory-2 & 3 (OCO-2 & 3) [10, 11], launched by NASA in July 2014 and May 2019, respectively, constitute the current state-of-the-art in space-based CO₂ observing systems. These instruments use the sunlight reflected off the Earth’s surface to infer the CO₂ concentration in the atmosphere below. Since the observations are indirect measurements of the quantity of interest, the task of estimating the atmospheric state, known as *retrieval* in remote sensing [33], is an ill-posed inverse problem [19, 13, 43]. The ultimate goal of these missions is to estimate the vertically averaged atmospheric CO₂ concentration at high precision in order

*PP and MK were supported by JPL subcontract no. 1629749. JH’s part of the research was carried out at the Jet Propulsion Laboratory, California Institute of Technology, under a contract with the National Aeronautics and Space Administration.

[†]Department of Statistics and Data Science and Machine Learning Department, Carnegie Mellon University, Pittsburgh, PA 15213 (pratik@cmu.edu).

[‡]Department of Statistics and Data Science, Carnegie Mellon University, Pittsburgh, PA 15213 (mkuusela@andrew.cmu.edu).

[§]Jet Propulsion Laboratory, California Institute of Technology, Pasadena, CA 91109 (jonathan.m.hobbs@jpl.nasa.gov).

to better understand the sources and sinks of CO₂ in the Earth system [8].

Estimating atmospheric CO₂ concentrations from space is a highly nontrivial task. Designing and building the required remote sensing instrument and developing the mathematical forward model for relating the scientifically relevant quantities to the actual satellite observations are both extremely challenging tasks [30]. However, statistically, the main complication arises from the fact that in order to go from the raw satellite observations to the CO₂ concentrations, one needs to solve the associated ill-posed inverse problem [6]. A satellite on low-Earth orbit is only able to measure CO₂ indirectly through the effect the gas has on the sunlight passing through the atmosphere. Information about CO₂ at different altitudes will therefore inevitably be convoluted in the raw observations. Inverting the forward model to obtain a reconstruction of the atmospheric CO₂ profile at different altitudes will hence result in highly oscillatory and uncertain solutions which, at first glance, may seem to have little scientific value.

The OCO-2 & 3 science teams are well-aware of these challenges and the operational missions essentially employ two strategies to circumvent the forward model ill-posedness [2]. First, the missions acknowledge that it is not feasible to retrieve the full vertical CO₂ profile from space. Instead, the missions have identified the vertically averaged CO₂ concentration, denoted by X_{CO_2} , as their primary quantity of interest, and the retrieval and validation efforts are focused on the accuracy and precision of this scalar quantity. Second, in order to estimate X_{CO_2} , the missions employ a strategy where first a regularized CO₂ profile is reconstructed (or more precisely, a regularized state vector containing the CO₂ profile and other retrieved atmospheric quantities), which then used to calculate the corresponding X_{CO_2} value. The regularization is achieved using a Bayesian inference framework where a prior distribution on the underlying state variables is used to promote physically plausible CO₂ profiles [2, 4, 5, 7]. The prior mean for the CO₂ vertical profile incorporates major large-scale variations in CO₂ over both space and time [2, 30]. Even so, regional biases are found in the retrieved X_{CO_2} when compared to ground-based validation sources [50, 21, 20, 49]. In this paper, we specifically focus on the question of how to rigorously quantify the uncertainty of the retrieved X_{CO_2} . We demonstrate that the existing retrieval procedure may lead to badly miscalibrated uncertainties for X_{CO_2} as a result of sizable, spatially correlated biases in the final X_{CO_2} estimates. We then show that it is possible to obtain more reliable prior-free uncertainties by adopting a frequentist approach that directly retrieves X_{CO_2} without the intermediate Bayesian regularization step.

To introduce some of the key ideas, it is worth considering a simplified version of the CO₂ retrieval problem (see Sections 2.2 and 5.1 for a description of the full problem). The retrieval problem is typically formulated in terms of an unknown state vector \mathbf{x} that includes both the vertical CO₂ profile of interest and other geophysical nuisance variables that affect the observations in the satellite. Assume that the state vector \mathbf{x} is related to the observations \mathbf{y} by the linear model $\mathbf{y} = \mathbf{K}\mathbf{x} + \boldsymbol{\varepsilon}$, where \mathbf{K} is a known forward operator dictated by the physics of the problem and $\boldsymbol{\varepsilon}$ represents stochastic noise in the measurement device with mean zero and covariance $\boldsymbol{\Sigma}_{\boldsymbol{\varepsilon}}$. The fundamental challenge here is that \mathbf{K} is an ill-conditioned matrix so that its singular values decay rapidly (in fact, exponentially, as evidenced in our experiments). Assume, for now, that \mathbf{K} has full column rank, and therefore the least-squares estimator of \mathbf{x} is given by $\hat{\mathbf{x}} = (\mathbf{K}^T \mathbf{K})^{-1} \mathbf{K}^T \mathbf{y}$. The covariance matrix of this estimator is

$\text{cov}(\hat{\mathbf{x}}) = (\mathbf{K}^T \mathbf{K})^{-1} \mathbf{K}^T \Sigma_\varepsilon \mathbf{K} (\mathbf{K}^T \mathbf{K})^{-1}$. Due to the ill-posedness of \mathbf{K} , the fluctuations in the noise ε get amplified in the inversion and the estimator $\hat{\mathbf{x}}$ exhibits large oscillations within the CO₂ profile that tend to be anti-correlated from one altitude to the next. This is also reflected in the covariance $\text{cov}(\hat{\mathbf{x}})$, and any confidence intervals derived for the individual CO₂ elements in \mathbf{x} based on $\text{cov}(\hat{\mathbf{x}})$ would be extremely wide, indicating, as they should, that the observations \mathbf{y} do not contain enough information to effectively constrain CO₂ at a given altitude. However, this should not deter us from trying to constrain *other functionals of \mathbf{x}* based on $\hat{\mathbf{x}}$. Of particular interest in our case is the vertically averaged CO₂ concentration given by the functional $X_{\text{CO}_2} = \mathbf{h}^T \mathbf{x}$, where \mathbf{h} is a known vector of weights (see Sections 2.2 and 5.1.1 for more details). The plug-in estimator of X_{CO_2} is $\hat{X}_{\text{CO}_2} = \mathbf{h}^T \hat{\mathbf{x}}$ with variance $\text{var}(\hat{X}_{\text{CO}_2}) = \mathbf{h}^T \text{cov}(\hat{\mathbf{x}}) \mathbf{h}$. Since the mapping from \mathbf{x} to X_{CO_2} is an averaging operation, one would expect that the anti-correlated fluctuations in the unregularized $\hat{\mathbf{x}}$ largely cancel out as it is mapped into \hat{X}_{CO_2} , resulting in a well-behaved estimator of X_{CO_2} with a reasonable variance. The X_{CO_2} results in [31] can be seen to suggest this and our results further confirm that this seems to be the case. When the noise ε is Gaussian, which is a good approximation here, one can then use the variance $\text{var}(\hat{X}_{\text{CO}_2})$ to construct a frequentist confidence interval around \hat{X}_{CO_2} . Assuming that the forward model is correctly specified, these intervals have guaranteed frequentist coverage for X_{CO_2} , *without assuming any prior knowledge of \mathbf{x}* . Arguably, these intervals provide the actual objective uncertainty of X_{CO_2} in the absence a priori information about \mathbf{x} .

The actual retrieval problem is more complex than the simplified situation described above. First, the forward operator relating the state vector \mathbf{x} to the observations \mathbf{y} is a nonlinear function of \mathbf{x} [2]. Second, there are known physical constraints on the state vector \mathbf{x} that should ideally be taken into account in the retrieval. For example, those elements of \mathbf{x} that correspond to CO₂ concentrations should be constrained to be non-negative. Third, the forward mapping need not be injective. This means, for example, that the matrices corresponding to a linearization of the forward mapping by, say, a Taylor expansion, may be rank deficient. In this paper, we address these last two complications in the case of a linearized approximation to the nonlinear forward operator. In other words, we seek to rigorously quantify the uncertainty of $X_{\text{CO}_2} = \mathbf{h}^T \mathbf{x}$ under the model $\mathbf{y} = \mathbf{K} \mathbf{x} + \varepsilon$, where \mathbf{K} need not have full column rank, $\mathbf{x} \in C$, where C is a set of known physical constraints (i.e., constraints that hold with probability 1), and ε is noise with known Gaussian statistics. We focus on the case where C corresponds to affine constraints on the elements of the state vector \mathbf{x} , and in particular, on the case of non-negativity constraints on certain elements of the state vector. Under this setup, we seek to construct $(1 - \alpha)$ frequentist confidence intervals for X_{CO_2} without imposing any other regularization on \mathbf{x} . We propose a procedure that is demonstrated to have nominal $(1 - \alpha)$ coverage in situations where the previous Bayesian procedure can be severely miscalibrated. Even though our procedure relies on much weaker prior information, the new intervals are not excessively wide since the problem is implicitly regularized by the choice of the functional $\mathbf{h}^T \mathbf{x}$ and the constraints $\mathbf{x} \in C$. These results lead us to conclude that the previous X_{CO_2} uncertainties can be unreliable, while the new method consistently provides well-calibrated uncertainty quantification.

We also investigate the potential implications of these results on CO₂ flux estimates [12] by studying the behavior of the different methods over a small spatial domain. We find that

with the operational Bayesian retrievals, the interaction between the regularizing prior and the spatially dependent true state vectors leads to a situation where the miscalibration of the X_{CO_2} intervals varies in a spatially coherent fashion. These intervals can have systematic offsets and, depending on the magnitude of these offsets, the reported uncertainties may either be systematically too small or too large over a given spatial region. It is possible that retrievals with such uncertainties could lead to spurious CO_2 flux estimates in downstream analyses. On the other hand, the sampling properties of the proposed frequentist intervals do not vary spatially, which makes them arguably more suitable for downstream scientific use.

In addition, we study the contributions of individual state vector elements to the X_{CO_2} uncertainty, identifying surface pressure and a certain aerosol variable as the key parameters that contribute most to the final uncertainty. This means that the X_{CO_2} uncertainty could potentially be further reduced if additional external information was available to constrain these two variables. We then provide a principled framework for incorporating such information in either deterministic or probabilistic forms into our method and investigate the extent to which such additional information on surface pressure reduces the X_{CO_2} uncertainty in our retrievals.

This work relates to the wider discussion on uncertainty quantification in ill-posed inverse problems (see, e.g., [39, 40, 44, 42]). In applied situations, uncertainty quantification in inverse problems tends to be dominated by Bayesian approaches that regularize the problem using a prior distribution. This is certainly the case in atmospheric sounding [33], but also in other domain sciences (e.g., [1, 19, 18, 26, 46, 48]). Penalized frequentist techniques, such as penalized maximum likelihood or Tikhonov regularization (also known as ridge regression in the statistics literature [17]), are closely related to Bayesian approaches since one can usually interpret the penalty term as corresponding to a Bayesian log-prior (see, e.g., Sections 7.5 and 7.6 in [27]). These techniques are problematic from the perspective of frequentist uncertainty quantification since the intervals they produce tend to be systematically offset from the true value of the unknown quantity due to the bias that regularizes the problem. This can lead to drastic undercoverage for these intervals [23, 24, 22]. There exists, however, a lesser-known line of work (see [37, 36, 35] and the references therein) that attempts to construct truly frequentist confidence intervals in ill-posed problems. The key is to use physically known *objective constraints* to regularize the problem instead of a subjective Bayesian prior. This enables deriving intervals with *guaranteed frequentist coverage* [37, 38]. This paper builds upon these ideas, but adds to the discussion the important role of the functional of interest in regularizing the problem. We also focus on intervals which are designed to constrain one functional at a time, which is in contrast to some previous techniques [37, 24] that provide simultaneous intervals for *all* functionals at once, leading to substantial overcoverage if only one or a small subset of functionals is needed. We highlight the importance of choosing the functional of interest wisely so that it circumvents the ill-posedness of the problem, while still providing scientifically useful information. We demonstrate that, given such a functional and mild, readily available physical constraints, it is possible to construct intervals that perform well in terms of both length and coverage. These intervals have neither the undercoverage of the Bayesian/penalized techniques nor the overcoverage of the simultaneous frequentist intervals and can therefore be attractive in a wide range of applications in which there is a single quantity of interest, such as the CO_2 retrieval problem considered in this paper.

The rest of this paper is organized as follows. To set up the problem, we briefly describe the physics of observing CO₂ from space and the corresponding statistical model in Section 2. Next, we outline the existing operational retrieval procedure and analyze its properties in Section 3. We then describe the proposed frequentist uncertainty quantification method and discuss its properties in Section 4. Section 5 compares the coverage performance of the operational and proposed procedures both for an individual sounding location and over a small spatial region using simulated data from a realistic generative model. In Section 6, we further investigate the proposed method to better understand the impact of the individual state vector elements on the final interval length, and provide a framework to incorporate additional deterministic or probabilistic constraints into our method. Finally, Section 7 offers concluding remarks and directions for future work. The appendices contain derivations and other technical results.

2. Problem background and setup.

2.1. Remote sensing of carbon dioxide. Remote sensing of atmospheric CO₂ is feasible due to the absorption of solar radiation by CO₂ molecules at specific wavelengths, particularly in the infrared (IR) portion of the electromagnetic spectrum. In this part of the spectrum, variations in the observed top-of-the-atmosphere radiation can also be induced by other surface and atmospheric properties, including albedo (surface reflectivity), absorption by other atmospheric trace gases, and absorption and scattering in the presence of clouds and aerosol particles. These processes are illustrated schematically in Figure 1. These additional effects explain most of the variation in the radiance (intensity of the observed radiation) that is seen by a downward looking satellite at the top of the atmosphere. Radiance changes due to variation in CO₂ are more subtle. CO₂-focused remote sensing instruments, such as OCO-2 & 3, therefore require high-precision radiance observations at fine spectral resolution. The OCO-2 and OCO-3 instruments are duplicates of the same design. Each instrument includes three imaging grating spectrometers that each correspond to a narrow IR band. These are the O₂ A-band centered around 0.765 μm , the weak CO₂ band centered around 1.61 μm , and the strong CO₂ band centered near 2.06 μm . The O₂ A-band includes numerous absorption lines for atmospheric O₂, and the two CO₂ bands include absorption lines for CO₂ [2].

A collection of observed radiances at a particular time and location is known as a *sounding*. For OCO-2 & 3, a sounding includes 1016 radiances in each of the three spectral bands. Figure 2 depicts an example sounding for OCO-2. The fine wavelength spacing within each band ensures the ability to resolve individual absorption features. Since atmospheric O₂ has a nearly constant fractional abundance of 0.209, the absorption in the O₂ A-band can be used to estimate the total amount of dry air in the atmospheric column, which is sometimes termed as the radiative path length. In the retrieval, this is formally represented by retrieving the atmospheric surface pressure. This can be combined with the absolute absorption in the CO₂ bands to estimate the relative abundance, or dry-air mole fraction, of CO₂. In addition, the A-band in particular has sensitivity to cloud and aerosol scattering, which are also estimated in the retrieval process.

While the instruments themselves are nearly identical, OCO-2 and OCO-3 have different observing patterns. OCO-2 is in a polar orbit as part of a satellite constellation known as the A-train with observations collected exclusively in the early afternoon local time [2].

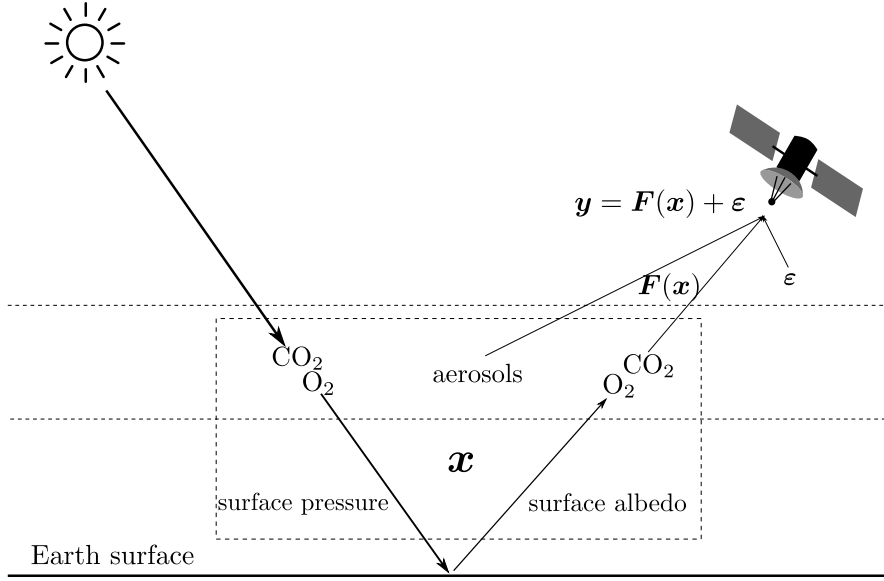


Figure 1. Schematic of space-based CO₂ sensing in the OCO-2 mission.

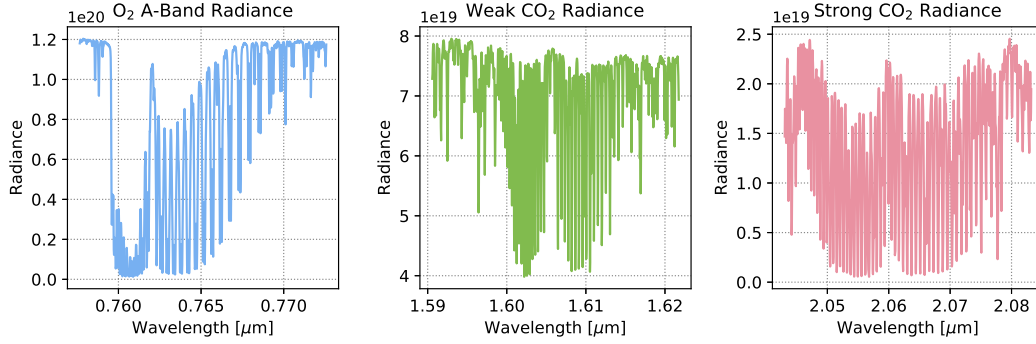


Figure 2. Example sounding from OCO-2. A sounding includes 1016 radiances in each of the three infrared spectral bands.

OCO-3 has recently been installed on the International Space Station (ISS) and is collecting observations in tropical and mid-latitude regions at varying times of the day following the ISS precessing orbit [11]. In the rest of this paper, we primarily focus on OCO-2, but we expect our conclusions to also apply to OCO-3 due to the similarity of the two instruments.

2.2. Mathematical model. The physical model for CO₂ remote sensing as illustrated in Figure 1 can be mathematically written down as

$$(2.1) \quad \mathbf{y} = \mathbf{F}(\mathbf{x}) + \epsilon,$$

where $\mathbf{x} \in \mathbb{R}^p$ is an unknown state vector, $\mathbf{y} \in \mathbb{R}^n$ is a vector of observed radiances, $\mathbf{F} : \mathbb{R}^p \rightarrow \mathbb{R}^n$ models the physical processes described in Section 2.1 that relate the state

vector to the expected radiances and $\boldsymbol{\varepsilon}$ represents zero-mean instrument noise. For the OCO-2 mission, we have $n \gg p$. Despite this, the problem of retrieving \boldsymbol{x} based on \boldsymbol{y} is badly ill-posed due to poor conditioning of \boldsymbol{F} .

The ultimate goal of the retrieval is to estimate a certain functional of the state vector $\theta(\boldsymbol{x}) \in \mathbb{R}$ using the observations \boldsymbol{y} . In the case of OCO-2, the state vector \boldsymbol{x} contains all the physical quantities that are thought to affect the radiance measurement \boldsymbol{y} . This includes the vertical CO₂ concentrations, but also other geophysical quantities, as described in Section 2.1. Statistically, these other quantities can be understood as nuisance variables since the functional of interest does not directly depend on them.

The actual full-physics forward operator \boldsymbol{F} is a non-linear map from \mathbb{R}^p to \mathbb{R}^n [2]. In addition, there could be misspecification in the forward model (2.1) from multiple sources, including missing nuisance variables and non-Gaussian noise. The functional of interest also has a mild nonlinearity to it [15]. These complications can detract from the fundamental challenges involved in quantifying the uncertainty of the retrievals. In order to be able to focus on the key statistical issues, we make in this paper the following assumptions and simplifications:

1. *State vector:* We assume that, in addition to the variables of interest (i.e., the vertical profile of CO₂ concentrations), the state vector \boldsymbol{x} contains all the relevant nuisance variables. See Section 5.1.1 for the particular set of nuisance variables we use in the numerical experiments.
2. *Forward operator:* We linearize the forward operator $\boldsymbol{F}(\boldsymbol{x})$ at a particular $\boldsymbol{x} = \boldsymbol{x}'$ such that $\boldsymbol{F}(\boldsymbol{x}) \approx \boldsymbol{K}\boldsymbol{x} + \boldsymbol{F}(\boldsymbol{x}') - \boldsymbol{K}\boldsymbol{x}'$, where $\boldsymbol{K} = \left. \frac{\partial \boldsymbol{F}(\boldsymbol{x})}{\partial \boldsymbol{x}} \right|_{\boldsymbol{x}=\boldsymbol{x}'}$ is the Jacobian of \boldsymbol{F} evaluated at \boldsymbol{x}' .
3. *Noise:* We assume a Gaussian distribution for the noise $\boldsymbol{\varepsilon}$ so that $\boldsymbol{\varepsilon} \sim \mathcal{N}(\mathbf{0}, \boldsymbol{\Sigma}_{\boldsymbol{\varepsilon}})$ with a diagonal covariance matrix $\boldsymbol{\Sigma}_{\boldsymbol{\varepsilon}}$. This constitutes using a Gaussian approximation to the Poisson-like noise in the actual satellite; see Section 5.1.2.
4. *Functional of interest:* The functional of interest is assumed to be linear so it can be written in the form $\theta = \boldsymbol{h}^T \boldsymbol{x}$, where the weights \boldsymbol{h} are assumed to be known. We specifically focus on θ corresponding to X_{CO_2} , the column-averaged CO₂ concentration at the sounding location, which, to a good approximation, is of this form.

Up to minor technical details, assumptions 1, 3 and 4 are similar to the current OCO-2 operational retrieval method; however, the operational procedure does take into account the nonlinearity of the forward operator. Even so, the operational uncertainty estimate uses a linearization about the final solution [2].

Putting these assumptions together, we have the following Gaussian linear model:

$$(2.2) \quad \boldsymbol{y}' = \boldsymbol{K}\boldsymbol{x} + \boldsymbol{\varepsilon}, \quad \boldsymbol{\varepsilon} \sim \mathcal{N}(\mathbf{0}, \boldsymbol{\Sigma}_{\boldsymbol{\varepsilon}}),$$

where $\boldsymbol{y}' = \boldsymbol{y} - \boldsymbol{F}(\boldsymbol{x}') + \boldsymbol{K}\boldsymbol{x}'$. To simplify the notation, we denote \boldsymbol{y}' as \boldsymbol{y} in the rest of this paper. Under this model, our goal is to obtain a $(1 - \alpha)$ confidence interval of the form $[\underline{\theta}, \bar{\theta}]$ for the functional $\theta = \boldsymbol{h}^T \boldsymbol{x}$ with the frequentist coverage guarantee $\mathbb{P}_{\boldsymbol{\varepsilon}}(\theta \in [\underline{\theta}, \bar{\theta}]) \approx 1 - \alpha$ for any \boldsymbol{x} , where $(1 - \alpha)$ is the desired confidence level and the probability statement is with respect to the distribution of the noise $\boldsymbol{\varepsilon}$.

3. Existing operational retrieval procedure.

3.1. Motivation. The existing OCO-2 operational retrieval procedure is based on a Bayesian maximum a posteriori estimator [2, 33]. The key idea in Bayesian retrievals is to let a prior distribution on the state vector \mathbf{x} regularize the problem. Prior domain knowledge about the state \mathbf{x} is incorporated in the form of a probability distribution, whose choice is always at least somewhat subjective and often informed by mathematical convenience rather than actual physical information. In remote sensing literature, this approach is called “optimal estimation” [33], although optimality here depends on the choice of a cost function and typically assumes that the prior is correctly specified. We describe below the Bayesian retrieval for our simplified setup with a linearized forward model. In the actual Full Physics operational retrievals with a nonlinear forward operator, finding the maximum of the posterior is a nonlinear optimization problem which is solved using the iterative Levenberg–Marquardt algorithm [2].

3.2. Method outline. The existing operational method for estimation and uncertainty quantification assumes a Gaussian prior distribution for \mathbf{x} ,

$$(3.1) \quad \mathbf{x} \sim \mathcal{N}(\boldsymbol{\mu}_a, \boldsymbol{\Sigma}_a),$$

where $\boldsymbol{\mu}_a$ and $\boldsymbol{\Sigma}_a$ are the prior mean and covariance, respectively. The posterior under this assumption and the linear forward model (2.2) is also Gaussian and given by

$$(3.2) \quad \mathbf{x}|\mathbf{y} \sim \mathcal{N}((\mathbf{K}^T \boldsymbol{\Sigma}_\varepsilon^{-1} \mathbf{K} + \boldsymbol{\Sigma}_a^{-1})^{-1}(\mathbf{K}^T \boldsymbol{\Sigma}_\varepsilon^{-1} \mathbf{y} + \boldsymbol{\Sigma}_a^{-1} \boldsymbol{\mu}_a), (\mathbf{K}^T \boldsymbol{\Sigma}_\varepsilon^{-1} \mathbf{K} + \boldsymbol{\Sigma}_a^{-1})^{-1}).$$

The estimator $\hat{\mathbf{x}}$ of \mathbf{x} is chosen to be the maximizer of the posterior distribution,

$$\hat{\mathbf{x}} = (\mathbf{K}^T \boldsymbol{\Sigma}_\varepsilon^{-1} \mathbf{K} + \boldsymbol{\Sigma}_a^{-1})^{-1}(\mathbf{K}^T \boldsymbol{\Sigma}_\varepsilon^{-1} \mathbf{y} + \boldsymbol{\Sigma}_a^{-1} \boldsymbol{\mu}_a),$$

which in our simplified setup is also the posterior mean.

Recalling that $\mathbf{y} = \mathbf{K}\mathbf{x} + \boldsymbol{\varepsilon}$, this estimator can be written as a sum of three terms, $\hat{\mathbf{x}} = \hat{\mathbf{x}}_1 + \hat{\mathbf{x}}_2 + \hat{\mathbf{x}}_3$, where the individual terms are as follows:

$$\begin{aligned} \hat{\mathbf{x}}_1 &= (\mathbf{K}^T \boldsymbol{\Sigma}_\varepsilon^{-1} \mathbf{K} + \boldsymbol{\Sigma}_a^{-1})^{-1} \mathbf{K}^T \boldsymbol{\Sigma}_\varepsilon^{-1} \mathbf{K} \mathbf{x} = \mathbf{A} \mathbf{x}, \\ \hat{\mathbf{x}}_2 &= (\mathbf{K}^T \boldsymbol{\Sigma}_\varepsilon^{-1} \mathbf{K} + \boldsymbol{\Sigma}_a^{-1})^{-1} \boldsymbol{\Sigma}_a^{-1} \boldsymbol{\mu}_a = (\mathbf{I} - \mathbf{A}) \boldsymbol{\mu}_a, \\ \hat{\mathbf{x}}_3 &= (\mathbf{K}^T \boldsymbol{\Sigma}_\varepsilon^{-1} \mathbf{K} + \boldsymbol{\Sigma}_a^{-1})^{-1} \mathbf{K}^T \boldsymbol{\Sigma}_\varepsilon^{-1} \boldsymbol{\varepsilon} = \mathbf{G} \boldsymbol{\varepsilon}, \end{aligned}$$

where $\mathbf{G} = (\mathbf{K}^T \boldsymbol{\Sigma}_\varepsilon^{-1} \mathbf{K} + \boldsymbol{\Sigma}_a^{-1})^{-1} \mathbf{K}^T \boldsymbol{\Sigma}_\varepsilon^{-1}$ and $\mathbf{A} = \mathbf{G} \mathbf{K}$ are called the retrieval gain matrix and the averaging kernel matrix, respectively [33].

The estimator for $\theta = \mathbf{h}^T \mathbf{x}$ is chosen to be the plug-in estimator $\hat{\theta} = \mathbf{h}^T \hat{\mathbf{x}}$, which again can be broken down into the respective three terms $\hat{\theta} = \hat{\theta}_1 + \hat{\theta}_2 + \hat{\theta}_3$ where $\hat{\theta}_i = \mathbf{h}^T \hat{\mathbf{x}}_i$. Observe that the components $\hat{\mathbf{x}}_2$ and $\hat{\theta}_2$ are fixed and do not depend on either the true state \mathbf{x} or the noise $\boldsymbol{\varepsilon}$. The components $\hat{\mathbf{x}}_1$ and $\hat{\theta}_1$ depend on the true state, whereas the remaining components $\hat{\mathbf{x}}_3$ and $\hat{\theta}_3$ depend on the noise.

Finally, to quantify the uncertainty of estimating θ , we note that the posterior distribution on \mathbf{x} induces a Gaussian posterior distribution on θ given by

$$(3.3) \quad \theta|\mathbf{y} \sim \mathcal{N}(\mathbf{h}^T (\mathbf{K}^T \boldsymbol{\Sigma}_\varepsilon^{-1} \mathbf{K} + \boldsymbol{\Sigma}_a^{-1})^{-1} (\mathbf{K}^T \boldsymbol{\Sigma}_\varepsilon^{-1} \mathbf{y} + \boldsymbol{\Sigma}_a^{-1} \boldsymbol{\mu}_a), \mathbf{h}^T (\mathbf{K}^T \boldsymbol{\Sigma}_\varepsilon^{-1} \mathbf{K} + \boldsymbol{\Sigma}_a^{-1})^{-1} \mathbf{h}).$$

An approximate $(1 - \alpha)$ confidence interval for θ is then given by the posterior credible interval

$$(3.4) \quad [\underline{\theta}, \bar{\theta}] = [\hat{\theta} - z_{1-\alpha/2}\sigma, \hat{\theta} + z_{1-\alpha/2}\sigma],$$

where $\sigma^2 = \mathbf{h}^T(\mathbf{K}^T \boldsymbol{\Sigma}_\varepsilon^{-1} \mathbf{K} + \boldsymbol{\Sigma}_a^{-1})^{-1} \mathbf{h}$ is the posterior variance of θ , $z_{1-\alpha/2}$ the $(1 - \alpha/2)$ standard normal quantile and $\hat{\theta}$ the plug-in estimator of θ , or equivalently the maximizer/mean of $p(\theta|\mathbf{y})$.

The credible interval (3.4) is used to quantify the uncertainty of X_{CO_2} in the operational OCO-2 retrievals [2]. It is worth noting that this credible interval is different from the standard error interval $[\hat{\theta} - z_{1-\alpha/2} \text{se}(\hat{\theta}), \hat{\theta} + z_{1-\alpha/2} \text{se}(\hat{\theta})]$, where $\text{se}(\hat{\theta}) = \sqrt{\text{var}_\varepsilon(\hat{\theta})}$ is the standard error of $\hat{\theta}$ and

$$(3.5) \quad \begin{aligned} \text{var}_\varepsilon(\hat{\theta}) &= \text{var}_\varepsilon(\hat{\theta}_3) = \text{var}_\varepsilon(\mathbf{h}^T \mathbf{G} \boldsymbol{\varepsilon}) = \mathbf{h}^T \mathbf{G} \boldsymbol{\Sigma}_\varepsilon \mathbf{G}^T \mathbf{h} \\ &= \mathbf{h}^T (\mathbf{K}^T \boldsymbol{\Sigma}_\varepsilon^{-1} \mathbf{K} + \boldsymbol{\Sigma}_a^{-1})^{-1} \mathbf{K}^T \boldsymbol{\Sigma}_\varepsilon^{-1} \mathbf{K} (\mathbf{K}^T \boldsymbol{\Sigma}_\varepsilon^{-1} \mathbf{K} + \boldsymbol{\Sigma}_a^{-1})^{-1} \mathbf{h} \end{aligned}$$

is the variance of $\hat{\theta}$ computed with respect to the distribution of the noise $\boldsymbol{\varepsilon}$. It is easy to show that the credible interval is always longer than the standard error interval. This extra length can be understood as an attempt to account for the regularization bias in the uncertainties; see Section 6.4 in [34] and the references therein.

3.3. Method properties. It is straightforward to derive the following properties for the linearized operational estimator $\hat{\theta}$ and the confidence interval $[\underline{\theta}, \bar{\theta}]$ given in Equation (3.4):

- *Bias:* The bias of the estimator $\hat{\theta}$, denoted by $\text{bias}(\hat{\theta})$, can be calculated as

$$(3.6) \quad \begin{aligned} \text{bias}(\hat{\theta}) &= \mathbb{E}_\varepsilon[\hat{\theta}] - \theta = \hat{\theta}_1 + \hat{\theta}_2 - \theta = \mathbf{h}^T (\hat{\mathbf{x}}_1 + \hat{\mathbf{x}}_2 - \mathbf{x}) \\ &= \mathbf{h}^T (\mathbf{A} \mathbf{x} + (\mathbf{I} - \mathbf{A}) \boldsymbol{\mu}_a - \mathbf{x}) = \mathbf{h}^T (\mathbf{A} - \mathbf{I})(\mathbf{x} - \boldsymbol{\mu}_a) \\ &= \mathbf{m}^T (\mathbf{x} - \boldsymbol{\mu}_a), \end{aligned}$$

where $\mathbf{m} = (\mathbf{A}^T - \mathbf{I}) \mathbf{h} = (\mathbf{K}^T \boldsymbol{\Sigma}_\varepsilon^{-1} \mathbf{K} (\mathbf{K}^T \boldsymbol{\Sigma}_\varepsilon^{-1} \mathbf{K} + \boldsymbol{\Sigma}_a^{-1})^{-1} - \mathbf{I}) \mathbf{h}$ is a vector of bias multipliers. We observe that the bias depends on $\mathbf{x} - \boldsymbol{\mu}_a$, i.e., the difference between the true state \mathbf{x} and the prior mean $\boldsymbol{\mu}_a$. Notice that the bias is 0 if and only if $\mathbf{x} = \boldsymbol{\mu}_a$ or $\mathbf{m} = \mathbf{0}$ or if the vector $\mathbf{x} - \boldsymbol{\mu}_a$ is orthogonal to \mathbf{m} . In other cases, depending on $\mathbf{x} - \boldsymbol{\mu}_a$ and how it interacts with the forward operator \mathbf{K} , the prior covariance $\boldsymbol{\Sigma}_a$, the noise covariance $\boldsymbol{\Sigma}_\varepsilon$ and the functional \mathbf{h} , there might be a positive or a negative bias.

- *Coverage:* The actual frequentist coverage of the interval $[\underline{\theta}, \bar{\theta}]$ can be written down in closed form and is given by

$$(3.7) \quad \begin{aligned} \mathbb{P}_\varepsilon(\theta \in [\underline{\theta}, \bar{\theta}]) &= \mathbb{P}_\varepsilon(\theta - \hat{\theta}_1 - \hat{\theta}_2 - z_{1-\alpha/2}\sigma \leq \hat{\theta}_3 \leq \theta - \hat{\theta}_1 - \hat{\theta}_2 + z_{1-\alpha/2}\sigma) \\ &= \Phi \left(\frac{\text{bias}(\hat{\theta})}{\text{se}(\hat{\theta})} + z_{1-\alpha/2} \frac{\sigma}{\text{se}(\hat{\theta})} \right) - \Phi \left(\frac{\text{bias}(\hat{\theta})}{\text{se}(\hat{\theta})} - z_{1-\alpha/2} \frac{\sigma}{\text{se}(\hat{\theta})} \right), \end{aligned}$$

where $\text{se}(\hat{\theta}) = \sqrt{\text{var}_\varepsilon(\hat{\theta})}$ is the standard error of $\hat{\theta}$; see Equation (3.5). The coverage depends on \mathbf{x} only through $\text{bias}(\hat{\theta})$. It is an even function of $\text{bias}(\hat{\theta})$ and the maximum

is obtained with $\text{bias}(\hat{\theta}) = 0$. In that case,

$$\begin{aligned} \mathbb{P}_{\varepsilon}(\theta \in [\underline{\theta}, \bar{\theta}]) &= \Phi\left(z_{1-\alpha/2} \frac{\sigma}{\text{se}(\hat{\theta})}\right) - \Phi\left(-z_{1-\alpha/2} \frac{\sigma}{\text{se}(\hat{\theta})}\right) \\ &> \Phi(z_{1-\alpha/2}) - \Phi(-z_{1-\alpha/2}) = 1 - \alpha, \end{aligned}$$

since $\sigma/\text{se}(\hat{\theta}) > 1$. In other words, the interval $[\underline{\theta}, \bar{\theta}]$ has overcoverage for $\text{bias}(\hat{\theta}) = 0$. It is also easy to see that the coverage is a strictly decreasing function of $|\text{bias}(\hat{\theta})|$. As $|\text{bias}(\hat{\theta})|$ increases, the coverage eventually crosses the nominal value $(1 - \alpha)$, followed by undercoverage. In the limit $|\text{bias}(\hat{\theta})| \rightarrow \infty$, the coverage becomes zero.

- *Length:* The interval $[\underline{\theta}, \bar{\theta}]$ has constant length given by $2z_{1-\alpha/2}\sigma$.

3.4. Commentary. The operational retrieval method is based on the well-established Bayesian framework where the observed data are combined with the prior distribution to obtain inferences in the form of the posterior distribution. This apparent simplicity disguises the fact that the performance of the method can depend critically on the choice of the prior distribution. For example, the estimator $\hat{\theta}$ would be unbiased if the prior mean was chosen to be equal to the true state, i.e., $\boldsymbol{\mu}_a = \boldsymbol{x}$, but this is unrealistic in practice as it would require knowing beforehand what the value of \boldsymbol{x} is. (The bias is also small if $\boldsymbol{x} - \boldsymbol{\mu}_a$ is nearly orthogonal to \boldsymbol{m} but this is equally unlikely to generally hold true.) At least some amount of bias is therefore always present, with the potential for arbitrarily large biases depending on how badly the prior is misspecified. Since the coverage of the intervals depends on the bias, this can result in wildly varying coverage performance. For small biases, the intervals overcover, i.e., $\mathbb{P}_{\varepsilon}(\theta \in [\underline{\theta}, \bar{\theta}]) > 1 - \alpha$, while for large biases the intervals undercover, i.e., $\mathbb{P}_{\varepsilon}(\theta \in [\underline{\theta}, \bar{\theta}]) < 1 - \alpha$. Irrespective of which of these two cases dominates, the intervals are bound to have some degree of miscalibration since it is unlikely that there would always be just the right amount of bias for nominal coverage. Unfortunately, it is also impossible to judge the coverage of the intervals without knowing the true \boldsymbol{x} . Therefore, for real soundings, it is impossible to tell if a given interval is well-calibrated or not. Ideally, roughly $100 \times (1 - \alpha)\%$ of soundings from a given OCO-2 orbit would cover their true X_{CO_2} values. However, this discussion shows that, for the current retrieval method, this fraction can be much smaller or much larger. What makes the situation even worse is that, in the real atmosphere, the nearby states \boldsymbol{x} are spatially and temporally correlated. Since the bias depends on $\boldsymbol{x} - \boldsymbol{\mu}_a$, this means that the biases, and therefore also the coverage values, are spatially and temporally correlated, which may lead to misleading inferences over extended spatial regions or temporal periods. These effects are analyzed in greater detail using a simulated example scenario in Section 5.

4. Proposed frequentist retrieval procedure.

4.1. Motivation. The key idea of our proposed method is to let known physical constraints and the functional of interest regularize the problem without imposing other external a priori beliefs about the state elements. This suffices for obtaining well-calibrated and reasonably sized confidence intervals, as long as the constraints hold with probability 1 and the functional is an operation, such as averaging or smoothing, that tends to reduce noise. The procedure is formulated in terms of convex optimization problems that find the upper and

lower endpoints of the confidence interval [35, 36, 37]. Below we first describe the procedure followed by a brief analysis of its properties. We provide two complementary perspectives to illustrate the idea, one from the point of view of optimization in the state space \mathbb{R}^p (referred to as the primal form of the optimization problem) and another from the perspective of optimization in the radiance space \mathbb{R}^n (referred to as the dual form of the optimization problem).

4.2. Method outline. Unlike the operational procedure, our proposed method directly constructs confidence intervals for the functional of interest $\theta = \mathbf{h}^T \mathbf{x}$. More specifically, the goal is to construct a $(1 - \alpha)$ confidence interval $[\underline{\theta}, \bar{\theta}]$ for θ under the model $\mathbf{y} \sim \mathcal{N}(\mathbf{K}\mathbf{x}, \mathbf{I})$ subject to external information on \mathbf{x} in the form of the affine constraint $\mathbf{A}\mathbf{x} \leq \mathbf{b}$ and without requiring \mathbf{K} to have full column rank. The linear forward model in Equation (2.2) can always be transformed into this form by taking the Cholesky factorization $\Sigma_\epsilon = \mathbf{L}\mathbf{L}^T$, calculating $\tilde{\mathbf{y}} = \mathbf{L}^{-1}\mathbf{y}$ and $\tilde{\mathbf{K}} = \mathbf{L}^{-1}\mathbf{K}$, and then redefining $\mathbf{y} \leftarrow \tilde{\mathbf{y}}$ and $\mathbf{K} \leftarrow \tilde{\mathbf{K}}$. The matrix \mathbf{A} and the vector \mathbf{b} can encode various types of affine constraints on the state vector elements: for example, non-negativity constraints for individual elements of \mathbf{x} , bound constraints for individual elements of \mathbf{x} , or affine constraints involving multiple elements of \mathbf{x} at once. The endpoints of the interval $[\underline{\theta}, \bar{\theta}]$ are obtained as the objective function values of two convex optimization problems. The convex programs are chosen so that the coverage $\mathbb{P}_\epsilon(\theta \in [\underline{\theta}, \bar{\theta}])$ is as close as possible to the nominal value $(1 - \alpha)$ for all \mathbf{x} satisfying the constraint $\mathbf{A}\mathbf{x} \leq \mathbf{b}$.

4.2.1. Primal point of view. The lower endpoint $\underline{\theta}$ is the optimal objective function value of the following minimization problem [35, 36]:

$$(4.1) \quad \begin{aligned} & \text{minimize} && \mathbf{h}^T \mathbf{x} \\ & \text{subject to} && \|\mathbf{y} - \mathbf{K}\mathbf{x}\|^2 \leq z_{1-\alpha/2}^2 + s^2, \\ & && \mathbf{A}\mathbf{x} \leq \mathbf{b}, \end{aligned}$$

where the slack factor s^2 is defined as the objective function value of the following program:

$$(4.2) \quad \begin{aligned} & \text{minimize} && \|\mathbf{y} - \mathbf{K}\mathbf{x}\|^2 \\ & \text{subject to} && \mathbf{A}\mathbf{x} \leq \mathbf{b}. \end{aligned}$$

The upper endpoint $\bar{\theta}$ is the optimal value of a similar maximization problem:

$$(4.3) \quad \begin{aligned} & \text{maximize} && \mathbf{h}^T \mathbf{x} \\ & \text{subject to} && \|\mathbf{y} - \mathbf{K}\mathbf{x}\|^2 \leq z_{1-\alpha/2}^2 + s^2, \\ & && \mathbf{A}\mathbf{x} \leq \mathbf{b}, \end{aligned}$$

where s^2 is again given by program (4.2).

To explain the intuition behind this construction, we start with the approach described in [37]. Consider the two sets $D = \{\mathbf{x} \in \mathbb{R}^p : \|\mathbf{y} - \mathbf{K}\mathbf{x}\|^2 \leq \chi_{n,1-\alpha}^2\}$, where $\chi_{n,1-\alpha}^2$ is the $(1 - \alpha)$ quantile of the χ^2 distribution with n degrees of freedom, and $C = \{\mathbf{x} \in \mathbb{R}^p : \mathbf{A}\mathbf{x} \leq \mathbf{b}\}$. Here D is a $(1 - \alpha)$ confidence set for the entire state vector \mathbf{x} and the set C encodes the feasible set of \mathbf{x} given the constraints. Therefore, the set $C \cap D$ is also a $(1 - \alpha)$ confidence set for \mathbf{x} . We can then use this confidence set to obtain a $(1 - \alpha)$ confidence interval for the

functional $\theta = \mathbf{h}^T \mathbf{x}$ by simply finding the extremal values of the functional over $C \cap D$ [37], which corresponds to problems (4.1) and (4.3) with $z_{1-\alpha/2}^2 + s^2$ replaced by $\chi_{n,1-\alpha}^2$. However, since this choice of D guarantees coverage for the entire vector \mathbf{x} , this construction produces simultaneously valid confidence intervals for any arbitrarily large collection of functionals of \mathbf{x} . Thus, for the one particular functional we primarily care about, it produces valid but typically excessively large intervals that are likely to have substantial overcoverage. The idea of the method above therefore is to shrink the set D by calibrating the radius appropriately. It is suggested in [35, 36] that the appropriate radius for one-at-a-time coverage, i.e., for obtaining coverage for a single target functional, is $z_{1-\alpha/2}^2 + s^2$, which is the radius used in the programs above. One of the goals of this paper is to study the appropriateness of this choice and in particular to demonstrate that the intervals defined by (4.1) and (4.3) are indeed well-calibrated in the X_{CO_2} retrieval problem.

When we calculate the intervals in practice, we improve the computing time by using a simplification of (4.1)–(4.3) that allows us to replace these programs by equivalent optimization problems involving p -variate norms instead of n -variate norms; see Appendix A for details. These simplified problems are then solved using the interior-point solvers in Matlab 2019a.

4.2.2. Dual point of view. To gain more insight into this construction, we next look at the Lagrangian dual [3] of problems (4.1) and (4.3). When the optimal objective function value of the dual program equals that of the primal program, the problem is said to satisfy strong duality. Since programs (4.1) and (4.3) are convex, strong duality is guaranteed if the norm constraint in (4.1) and (4.3) is strictly feasible (Eq. (5.27) in [3]). This is true if we assume that the minimizer of the slack problem (4.2) is attained, as any such minimizer is strictly feasible for the norm constraint.

Then, the lower endpoint $\underline{\theta}$ can also be obtained as the objective function value of the following program, which is derived starting from (4.1) in Appendix B:

$$(4.4) \quad \begin{aligned} & \text{maximize} && \mathbf{w}^T \mathbf{y} - \sqrt{z_{1-\alpha/2}^2 + s^2} \|\mathbf{w}\| - \mathbf{b}^T \mathbf{c} \\ & \text{subject to} && \mathbf{h} + \mathbf{A}^T \mathbf{c} - \mathbf{K}^T \mathbf{w} = \mathbf{0}, \\ & && \mathbf{c} \geq \mathbf{0}, \end{aligned}$$

where the optimization is over the variables $\mathbf{w} \in \mathbb{R}^n$ and $\mathbf{c} \in \mathbb{R}^q$, with q the number of affine constraints on \mathbf{x} , and s^2 is as defined above. The upper endpoint $\bar{\theta}$ is given by an analogous program which is dual to (4.3):

$$(4.5) \quad \begin{aligned} & \text{minimize} && \mathbf{w}^T \mathbf{y} + \sqrt{z_{1-\alpha/2}^2 + s^2} \|\mathbf{w}\| + \mathbf{b}^T \mathbf{c} \\ & \text{subject to} && \mathbf{h} - \mathbf{A}^T \mathbf{c} - \mathbf{K}^T \mathbf{w} = \mathbf{0}, \\ & && \mathbf{c} \geq \mathbf{0}. \end{aligned}$$

The dual perspective provides us more insight into the proposed interval $[\underline{\theta}, \bar{\theta}]$. To see this, consider the interval

$$(4.6) \quad [\underline{\mathbf{w}}^T \mathbf{y} - z_{1-\alpha/2} \|\underline{\mathbf{w}}\| - \mathbf{b}^T \underline{\mathbf{c}}, \bar{\mathbf{w}}^T \mathbf{y} + z_{1-\alpha/2} \|\bar{\mathbf{w}}\| + \mathbf{b}^T \bar{\mathbf{c}}].$$

As we show below, if $(\underline{\mathbf{w}}, \underline{\mathbf{c}})$ and $(\bar{\mathbf{w}}, \bar{\mathbf{c}})$ are any fixed elements of $\mathbb{R}^n \times \mathbb{R}^q$ satisfying the constraints in programs (4.4) and (4.5), respectively, then the above interval has correct

coverage $(1 - \alpha)$. This is true even when \mathbf{K} is rank deficient and under the constraint $\mathbf{A}\mathbf{x} \leq \mathbf{b}$ for \mathbf{x} . Therefore, it makes sense to find $(\underline{\mathbf{w}}, \underline{\mathbf{c}})$ and $(\overline{\mathbf{w}}, \overline{\mathbf{c}})$ within the appropriate constraint sets such that the lower endpoint is maximized and the upper endpoint is minimized so that the overall interval is as short as possible. This optimized interval would have correct coverage if the optimized variables did not depend on \mathbf{y} , but unfortunately that is not the case here. In order to account for this optimism, it is necessary to inflate the interval to preserve coverage. The method proposed in [35, 36] does this by replacing $z_{1-\alpha/2}$ with $\sqrt{z_{1-\alpha/2}^2 + s^2}$, where s^2 is the slack defined above.

4.3. Method properties.

- *Coverage:* The dual formulation enables us to gain some understanding of the coverage of the proposed interval. Consider a lower endpoint of the form $\underline{\theta} = \mathbf{w}^T \mathbf{y} - z_{1-\alpha/2} \|\mathbf{w}\| - \mathbf{b}^T \mathbf{c}$ for some fixed \mathbf{w} and \mathbf{c} satisfying the constraints in program (4.4). We can then bound the miscoverage probability as follows:

$$\begin{aligned}
\mathbb{P}_\varepsilon(\underline{\theta} \geq \theta) &= \mathbb{P}_\varepsilon(\mathbf{w}^T \mathbf{y} - z_{1-\alpha/2} \|\mathbf{w}\| - \mathbf{b}^T \mathbf{c} \geq \theta) \\
&= \mathbb{P}_\varepsilon(\mathbf{w}^T \mathbf{y} - \mathbf{w}^T \mathbf{K} \mathbf{x} - z_{1-\alpha/2} \|\mathbf{w}\| \geq \mathbf{h}^T \mathbf{x} - \mathbf{w}^T \mathbf{K} \mathbf{x} + \mathbf{b}^T \mathbf{c}) \\
&\stackrel{(1)}{\leq} \mathbb{P}_\varepsilon(\mathbf{w}^T \mathbf{y} - \mathbf{w}^T \mathbf{K} \mathbf{x} - z_{1-\alpha/2} \|\mathbf{w}\| \geq \mathbf{h}^T \mathbf{x} - \mathbf{w}^T \mathbf{K} \mathbf{x} + \mathbf{c}^T \mathbf{A} \mathbf{x}) \\
&\stackrel{(2)}{=} \mathbb{P}_\varepsilon(\mathbf{w}^T \mathbf{y} - \mathbf{w}^T \mathbf{K} \mathbf{x} - z_{1-\alpha/2} \|\mathbf{w}\| \geq 0) \\
&\stackrel{(3)}{=} \alpha/2,
\end{aligned}$$

where (1) follows from the constraints $\mathbf{A}\mathbf{x} \leq \mathbf{b}$ and $\mathbf{c} \geq \mathbf{0}$; (2) uses the fact that \mathbf{w} and \mathbf{c} need to satisfy the constraint $\mathbf{h} + \mathbf{A}^T \mathbf{c} - \mathbf{K}^T \mathbf{w} = \mathbf{0}$; and (3) utilizes the fact that $\mathbf{w}^T \mathbf{y} \sim \mathcal{N}(\mathbf{w}^T \mathbf{K} \mathbf{x}, \|\mathbf{w}\|^2)$ for any fixed \mathbf{w} . Thus, for fixed \mathbf{w} and \mathbf{c} that satisfy the constraints, we have $\mathbb{P}_\varepsilon(\underline{\theta} \geq \theta) \leq \alpha/2$. Similarly, for an upper endpoint of the form $\overline{\theta} = \mathbf{w}^T \mathbf{y} + z_{1-\alpha/2} \|\mathbf{w}\| + \mathbf{b}^T \mathbf{c}$, where \mathbf{w} and \mathbf{c} satisfy the constraints in program (4.5), we have $\mathbb{P}_\varepsilon(\theta \geq \overline{\theta}) \leq \alpha/2$. Combining the two, we have $\mathbb{P}_\varepsilon(\underline{\theta} \leq \theta \leq \overline{\theta}) \geq 1 - \alpha$, giving the desired coverage probability. Notice, however, that when we optimize over \mathbf{w} and \mathbf{c} , the optimized \mathbf{w} can depend on the observations \mathbf{y} , and hence, the distribution of $\mathbf{w}^T \mathbf{y}$ may no longer simply be the Gaussian distribution given above. To account for this, the method introduces the slack factor s^2 to inflate the interval. Proving that the inflated interval has correct coverage is not trivial since the slack s^2 itself is also a function of \mathbf{y} , but we demonstrate empirically in Section 5 that the coverage seems to be very close to the desired value $(1 - \alpha)$.

- *Length:* Since the optimization problems defining the interval depend on the observed data \mathbf{y} , these intervals can have variable length. Our experiments in Section 5 confirm that the interval lengths indeed do vary across \mathbf{y} realizations, but, in our experimental setup at least, the average length does not appear to change much across different state vectors \mathbf{x} .
- *Connection with classical intervals:* In the special case where \mathbf{K} has full column rank, i.e., $\text{rank}(\mathbf{K}) = p$, and there are no constraints on \mathbf{x} , the proposed interval reduces to the usual Gaussian standard error interval induced by the unregularized least-squares

estimator of \mathbf{x} . That is, in this special case, the solutions of problems (4.1) and (4.3) yield the interval $[\hat{\theta}_{\text{LS}} - z_{1-\alpha/2} \text{se}(\hat{\theta}_{\text{LS}}), \hat{\theta}_{\text{LS}} + z_{1-\alpha/2} \text{se}(\hat{\theta}_{\text{LS}})]$, where $\hat{\theta}_{\text{LS}} = \mathbf{h}^T \hat{\mathbf{x}}_{\text{LS}}$ is the induced estimator of θ , $\hat{\mathbf{x}}_{\text{LS}} = (\mathbf{K}^T \mathbf{K})^{-1} \mathbf{K}^T \mathbf{y}$ is the unregularized least-squares estimator of \mathbf{x} and $\text{se}(\hat{\theta}_{\text{LS}}) = \sqrt{\mathbf{h}^T (\mathbf{K}^T \mathbf{K})^{-1} \mathbf{h}}$ is the standard error of $\hat{\theta}_{\text{LS}}$. The proof is given in Appendix C. By standard arguments, this interval has exact $(1 - \alpha)$ coverage and will have reasonable length when the mapping $\mathbf{x} \mapsto \theta$ is an averaging or smoothing operation. It is also worth noting that in this special case the interval has fixed length. When \mathbf{K} is rank deficient and/or there are constraints on \mathbf{x} , the classical standard error interval no longer applies, but the proposed interval does. The proposed interval can therefore be seen as an extension of the classical unregularized interval to these more complex situations, which arise in the X_{CO_2} retrieval problem studied in detail in Section 5.

4.4. Commentary. The proposed method takes advantage of the fact that certain functionals themselves provide enough regularity so that we can retrieve them with reasonably sized confidence intervals given only objectively known physical constraints and without resorting to using additional subjective knowledge. This way the method avoids dependence on subjective external beliefs for the coverage guarantees. In practice, these intervals tend to be better calibrated but longer than the operational intervals which rely on such subjective knowledge. In particular, intervals based on trivial physical constraints may sometimes be longer than desired. This can be alleviated if additional objective information about the state variables is available to shrink the constraint set. This information could come either in the form of additional hard constraints or in the form of soft constraints of coverage statements for some of the unknown variables. Since this method is designed to satisfy a frequentist coverage statement, it is possible to combine these different uncertainties to obtain a valid, shorter interval in the end. These variants are explored in Section 6.

5. Numerical results. In this section, we compare the performance of the linearized operational retrieval procedure and the proposed direct retrieval procedure. First, we explain the details of our experimental setup in Section 5.1. Then, we compare the frequentist coverage of the two methods for a single sounding location in Section 5.2 and over a small spatial region containing multiple soundings in Section 5.3.

5.1. Experiment setup.

5.1.1. Forward model and weight vector specifics. The starting point for our forward model is the OCO-2 surrogate model developed by Hobbs et al [15]. The surrogate model is a computationally efficient approximation to the OCO-2 Full Physics forward model [2]. Similar to the full model, it involves a nonlinear mapping from the state vector \mathbf{x} to the radiances \mathbf{y} , but is much faster to evaluate. The surrogate model also makes certain simplifications to the full OCO-2 state vector. To be able to study the fundamental statistical issues without additional complications, we make a further approximation by linearizing the surrogate model as described in Section 2.2. This leads to the linear model in Equation (2.2). The linearization is done around the generative process mean $\boldsymbol{\mu}_{\mathbf{x}}$; see Section 5.1.2.

The state vector \mathbf{x} in the surrogate model has 39 elements ($p = 39$) of which the first 20 correspond to the CO_2 profile and the remaining 19 are nuisance variables related to surface

pressure, surface albedo and atmospheric aerosol concentrations. The specific elements are as follows:

- Variables x_1, \dots, x_{20} are the dry-air mole fractions of atmospheric CO₂, i.e., the number of moles of CO₂ per one mole of dry air, in parts per million (ppm) at 20 fixed pressure levels. In the sequel, we denote these as levels 1 to 20, with level 1 being highest in the atmosphere (pressure ~ 0.1 hPa) and level 20 being the surface.
- Variable x_{21} is the surface air pressure in hPa. It corresponds to the total weight of the air molecules in the atmospheric column.
- Variables x_{22}, \dots, x_{27} relate to surface albedo, i.e., the fraction of total incoming solar radiation reflected off the Earth’s surface. Albedo varies across the three OCO-2 spectral bands and also within each band. In the surrogate model, albedo is modeled as a linear function within each spectral band; see Section B.2 in [15]. The albedo for each band is therefore parameterized by an intercept and a slope which enter the state vector as nuisance variables (x_{22}, x_{24} , and x_{26} are the three intercepts and x_{23}, x_{25} , and x_{27} are the slopes).
- Variables x_{28}, \dots, x_{39} parameterize the atmospheric aerosol concentrations and distributions. The surrogate model assumes that there are 4 aerosol types, which have distinct absorption and scattering properties. The first two are location-dependent composite species. For our investigation, these are sulfate and dust. The latter two are two cloud species, one for ice clouds and another for liquid water clouds [2, 15]. Each type is parameterized by 3 parameters corresponding to the aerosol optical depth (AOD, i.e., the opaqueness of the aerosol species measured as the natural logarithm of the ratio of incoming to transmitted radiation) as well as the altitude and thickness of each aerosol layer. Variables x_{28}, x_{31}, x_{34} , and x_{37} are the log-AOD values, variables x_{29}, x_{32}, x_{35} , and x_{38} are the altitudes, and variables x_{30}, x_{33}, x_{36} , and x_{39} are the log-thicknesses.

These pieces of information suffice in order to capture, to a good approximation, the relation between the atmospheric CO₂ profile x_1, \dots, x_{20} and the observed radiances \mathbf{y} [15].

In addition to the state vector \mathbf{x} , the forward operator depends on additional parameters, most notably on the solar and satellite viewing geometries, which are assumed to be known during the retrieval. In our case, the forward model is evaluated for an OCO-2 orbit that took place in October 2015 near the Lamont, Oklahoma, Total Carbon Column Observing Network (TCCON) site (36.604°N, 97.486°W). The satellite is in the nadir observing mode, i.e., pointed toward the ground directly underneath its orbit.

We can investigate the ill-posedness of the CO₂ retrieval problem by studying the singular values of the linearized forward operator represented by the 3048×39 matrix \mathbf{K} . The singular values (not shown) decay exponentially indicating that the retrieval problem is severely ill-posed [14]. The smallest singular value deviates from the exponential decay which we take to indicate that \mathbf{K} is rank deficient with rank 38. Hence, there is a one-dimensional null space. The condition number (the ratio of the largest to the smallest (numerically) non-zero eigenvalue) is 3.62×10^{12} , consistent with a severely ill-posed problem.

The ultimate quantity of interest in the retrieval problem is the column-averaged CO₂ dry-air mole fraction $X_{\text{CO}_2} = \mathbf{h}^T \mathbf{x}$, where \mathbf{h} is a weight vector derived in [29]; see also [2]. Since X_{CO_2} only involves the CO₂ profile, the nuisance variables get weight zero, i.e., $h_{21} =$

$\dots = h_{39} = 0$. The remaining weights are strictly positive and sum to one, $\sum_{i=1}^{20} h_i = 1$, so statistically X_{CO_2} is a weighted average of the CO_2 concentrations x_1, \dots, x_{20} . In the Full Physics retrievals, the weights h_i have a slight dependence on the nuisance variables, but in the surrogate model the weights do not depend on the state vector. In practice, the surrogate model weights are almost constant for the intermediate pressure levels, $h_2 \approx \dots \approx h_{19} \approx 0.526 = 1/19$, while the weights for the boundary levels are approximately half of this, $h_1 \approx h_{20} \approx 0.263 = 1/2 \cdot 1/19$. The use of a vertical coordinate system normalized by surface pressure [29, 2] leads to nearly the same pressure weights globally; slight variations result from changes in atmospheric water vapor, since X_{CO_2} represents a dry-air mole fraction.

5.1.2. Data generation. Our investigations require a realistic generative model from which synthetic states and observations can be simulated. A suitable multivariate distribution for the state vector \mathbf{x} , as well as a model for the spatial dependence among state vectors in a small spatial region, is developed in [16]. Briefly, the approach uses actual retrieved state vectors near Lamont, OK, during the month of October 2015. This collection is part of the OCO-2 Level 2 diagnostic data products, available at the NASA Goddard Earth Science Data and Information Services Center (GES DISC, <https://disc.gsfc.nasa.gov/OCO-2>). These are combined with a simulation-based assessment of the retrieval error properties to estimate the state vector mean $\boldsymbol{\mu}_{\mathbf{x}}$ and the single-sounding covariance $\boldsymbol{\Sigma}_{\mathbf{x}}$ for this location and time.

Synthetic data are then generated through the following steps:

1. *State vector generation for a single sounding:* $\mathbf{x} \sim \mathcal{N}(\boldsymbol{\mu}_{\mathbf{x}}, \boldsymbol{\Sigma}_{\mathbf{x}})$. The single-sounding states are simulated from a multivariate Normal distribution with parameters estimated from OCO-2 data as noted above.
2. *State vector generation for grid sounding:* We also simulate states $\mathbf{x}(\mathbf{s}_i)$ on a grid of $i = 1, \dots, 64$ locations within an OCO-2 orbit. Following [16], we assume that this spatial process $\mathbf{x}(\cdot) \sim \text{GP}(\boldsymbol{\mu}(\cdot), \mathbf{C}(\cdot, \cdot))$ is a Gaussian process with a spatially constant mean function $\boldsymbol{\mu}(\cdot) = \boldsymbol{\mu}_{\mathbf{x}}$ and cross-covariance function $\mathbf{C}(\cdot, \cdot)$ defined as

$$C_{kl}(\mathbf{s}_i, \mathbf{s}_j) = \text{cov}(x_k(\mathbf{s}_i), x_l(\mathbf{s}_j)) = \Sigma_{\mathbf{x},kl} \mathcal{M}_{kl}(\|\mathbf{s}_i - \mathbf{s}_j\|),$$

where \mathcal{M}_{kl} is a Matérn-type correlation function [41]. The smoothness and range parameters of the correlation function vary across k and l in a way that guarantees positive definiteness and were estimated from the above collection of OCO-2 retrieved state vectors [16].

3. *Noise generation:* $\boldsymbol{\varepsilon} \sim \mathcal{N}(\mathbf{0}, \boldsymbol{\Sigma}_{\boldsymbol{\varepsilon}})$. The OCO-2 radiances are fundamentally photon counts in the detectors so these measurements have Poisson-like behavior. The noise can nevertheless be approximated well using an additive Gaussian noise term with zero mean and variance proportional to the mean signal. Following [15] and [25], we let $\boldsymbol{\Sigma}_{\boldsymbol{\varepsilon}}$ be diagonal with elements

$$\text{var}(\varepsilon_j) = c_{b(j)} F_j(\boldsymbol{\mu}_{\mathbf{x}}),$$

where $b : \{1, \dots, 3048\} \rightarrow \{1, 2, 3\}$, $j \mapsto b(j)$ indicates the spectral band (O_2 , weak CO_2 , strong CO_2) of j , c_i are band-specific constants set to obtain signal-to-noise ratios comparable to the OCO-2 instrument and $F_j(\cdot)$ is the j th element of the forward

operator output. The ε realizations are i.i.d. both across repetitions of the experiment for a fixed state \mathbf{x} and over the different spatial sounding locations.

4. *Observation:* $\mathbf{y} = \mathbf{K}\mathbf{x} + \varepsilon$, where \mathbf{x} and ε are given by the previous steps. As noted in Section 5.1.1, the matrix \mathbf{K} results from linearizing the forward operator \mathbf{F} about the true mean $\boldsymbol{\mu}_{\mathbf{x}}$.

In addition, the operational procedure posits a prior distribution on the state \mathbf{x} , which is given by $\mathbf{x} \sim \mathcal{N}(\boldsymbol{\mu}_a, \boldsymbol{\Sigma}_a)$. We use the prior mean $\boldsymbol{\mu}_a$ and prior covariance $\boldsymbol{\Sigma}_a$ derived from the OCO-2 operational prior near Lamont, OK, in October 2015.

An important point to highlight is that $\boldsymbol{\mu}_a \neq \boldsymbol{\mu}_{\mathbf{x}}$ and $\boldsymbol{\Sigma}_a \neq \boldsymbol{\Sigma}_{\mathbf{x}}$. For OCO-2, the prior mean $\boldsymbol{\mu}_a$ varies in space and time but is dependent in part on climatology and expert knowledge. Further, $\boldsymbol{\Sigma}_a$ is the same for all retrievals. Therefore, the true conditions, represented through $\boldsymbol{\mu}_{\mathbf{x}}$ and $\boldsymbol{\Sigma}_{\mathbf{x}}$ in our simulations, will be different from the prior mean and covariance. This misspecification is a real challenge for the operational retrievals and a source of bias [28].

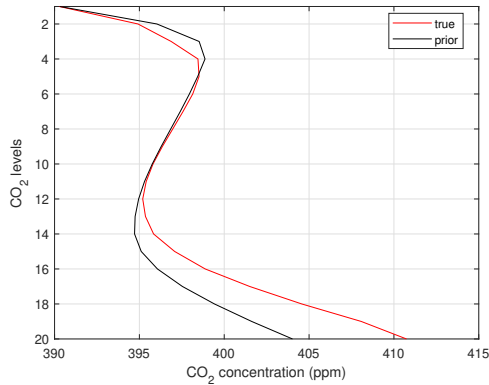
5.1.3. Exploratory analysis. We proceed to visualize and describe various components of the generative model and to compare those to the prior model. We begin by comparing the prior mean and standard deviation to the true generative model mean and standard deviation for the CO₂ part of the state vector in Figure 3. We observe that both the mean and the standard deviation have the largest misspecification near the surface. Table 1 contains the same information for the nuisance variables x_{21}, \dots, x_{39} . Generally speaking, the prior standard deviation is by design larger than that of the true process, which provides some protection against the prior mean misspecification.

We next visualize the correlation structure in the generative process and the prior. Figure 4(a) shows a heat map of the correlation matrix for the true generative process. We observe that the state vector consists of four independent subgroups of variables corresponding to the CO₂ profile, surface pressure, albedo variables and aerosol variables. While variables across these groups are uncorrelated, there are large within-group correlations. Figure 4(b) shows a heat map of the correlation matrix for the prior process. Again, the CO₂ variables are independent of the nuisance variables, but in this case, there are no correlations between the nuisance variables. Notice also the differences in the correlation structure within the CO₂ profile between the generative process and the prior.

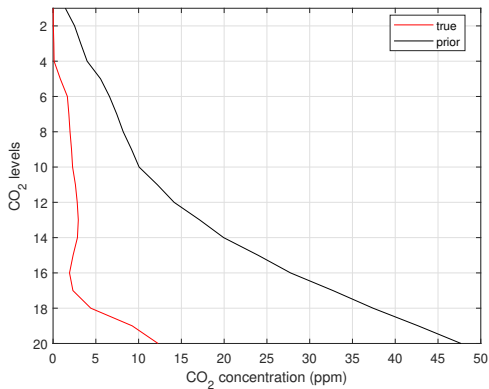
Lastly, we visualize the spatial correlation structure for the generative process over an 8×8 spatial grid near Lamont, OK. These 64 sounding locations are shown in Figure 5(a) and Figure 5(b) displays the correlations across the locations along the diagonal in Figure 5(a). Nearby state vectors are strongly spatially correlated, but there is a fair amount of decorrelation when moving across the grid.

5.1.4. Constraints. In the proposed frequentist procedure, we impose non-negativity constraints on certain elements of the state vector \mathbf{x} . Since elements x_1, \dots, x_{20} are CO₂ concentrations, they need to be non-negative by definition. Thus, we impose the constraint $x_i \geq 0$ for $i = 1, \dots, 20$. The same argument applies to surface pressure so we also include the constraint $x_{21} \geq 0$. The rest of the state vector elements are left unconstrained.

Since albedo is a fraction between 0 and 1, this implies in principle linear inequality constraints for the albedo intercepts and slopes x_{22}, \dots, x_{27} . We experimented with adding these constraints but found that that made little difference in the results while causing some



(a) Mean misspecification



(b) Standard deviation misspecification

Figure 3. Visualization of the misspecification of the mean and the standard deviation for the CO_2 profile between the true generative process and the prior. Figure (a) visualizes the misspecification in the mean and Figure (b) shows the misspecification in the standard deviation.

Table 1

Comparison of the true and prior mean and standard deviation for the nuisance variables x_i , $i = 21, \dots, 39$. A detailed description of these variables is given in Section 5.1.1.

i	true mean (sd)	prior mean (sd)
surface pressure		
21	972.3235 (1.7508)	970.6240 (4.000)
albedo		
22	0.1267 (0.0204)	0.1267 (1.0000)
23	0.0001 (0.0001)	0.0000 (0.0005)
24	0.2484 (0.0044)	0.2484 (1.0000)
25	-0.0001 (0.0000)	0.0000 (0.0005)
26	0.2027 (0.0026)	0.2027 (1.0000)
27	-0.0000 (0.0000)	0.0000 (0.0005)
aerosols		
28	-3.8786 (0.3380)	-3.7643 (2.0000)
29	0.8187 (0.0683)	0.9000 (0.2000)
30	-2.4492 (0.0409)	-2.9957 (0.1823)
31	-6.1959 (0.8492)	-4.7370 (2.0000)
32	0.3255 (0.0101)	0.9000 (0.2000)
33	-3.9219 (0.0201)	-2.9957 (0.1823)
34	-4.3980 (0.2477)	-4.3820 (1.8000)
35	-0.0087 (0.0355)	0.3000 (0.2000)
36	-3.2080 (0.0112)	-3.2189 (0.2231)
37	-5.6803 (0.2517)	-4.3820 (1.8000)
38	1.0917 (0.0870)	0.7500 (0.4000)
39	-2.3052 (0.0004)	-2.3026 (0.0953)

extra computational overhead. We therefore decided to leave these variables unconstrained. The aerosol variables x_{28}, \dots, x_{39} are parameterized in the surrogate model in such a way that there are no trivial constraints that could be imposed on those variables.

5.2. Single sounding.

5.2.1. Distribution of bias of the operational method. Since the linearized operational method is based on a linear estimator $\hat{\theta}$, we can write down $\text{bias}(\hat{\theta}) = \mathbb{E}_\epsilon[\hat{\theta}] - \theta$ in closed form for a given \mathbf{x} . This is done in Equation (3.6), which shows that the bias is given by the inner product of the bias multiplier vector \mathbf{m} and the prior mean misspecification $\mathbf{x} - \boldsymbol{\mu}_a$. For a given \mathbf{x} sampled from the generative model, there will therefore always be nonzero bias whose size depends on the details of the prior misspecification for that particular \mathbf{x} . To understand this interaction better, we show the bias multiplier vector \mathbf{m} in Figure 6(a) for

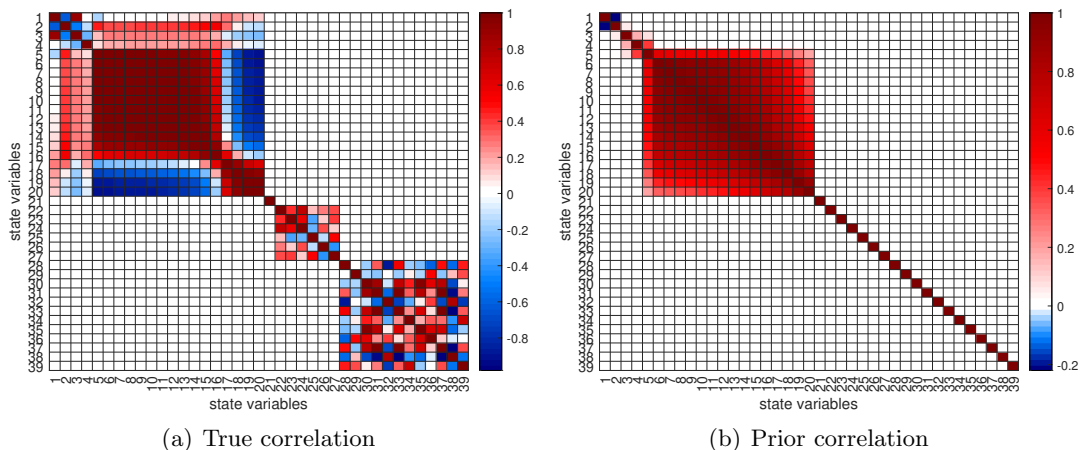


Figure 4. Visualization of the misspecification of the correlation structure between the true generative process and the prior. Figure (a) displays the correlation between the state vector elements in the true generative process. Figure (b) shows the same for the prior process.

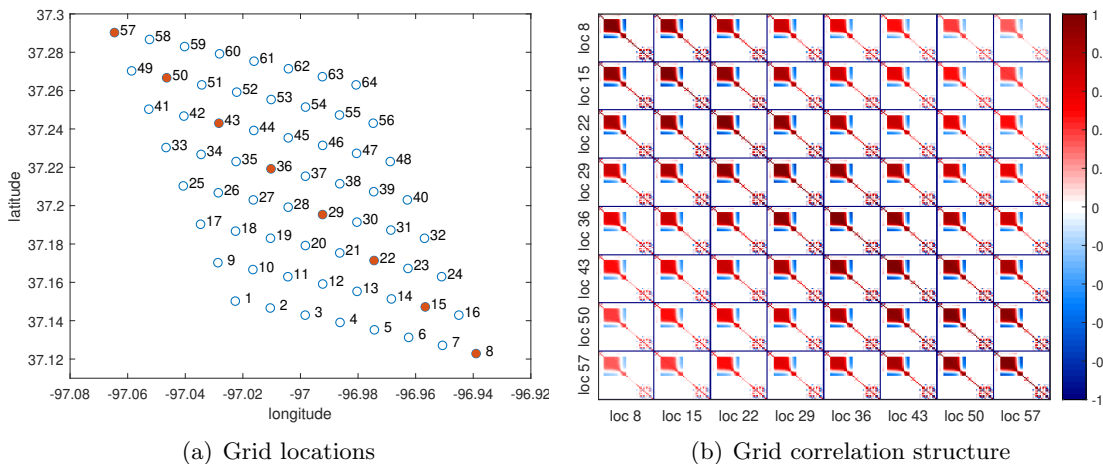


Figure 5. Visualization of the correlation structure between the state vector elements for the generative process over an 8×8 spatial grid. Figure (a) shows the coordinates of the sounding locations near Lamont, OK, with the numbers giving an index for each location. Figure (b) visualizes the correlation structure between the state vector elements across the marked locations along the diagonal in Figure (a). Notice the nonlinear color scale in Figure (b).

our particular retrieval setup. This highlights the role of the nuisance variables x_{21}, \dots, x_{39} in dictating the size of the bias. It is worth noting that the bias multiplier m depends on the prior covariance Σ_a but not on the prior mean μ_a . Hence this can be seen as a way of decoupling the contribution of the prior mean on the bias from that of the prior covariance.

Assuming that $\mathbf{x} \sim \mathcal{N}(\mu_{\mathbf{x}}, \Sigma_{\mathbf{x}})$ gives a realistic distribution of \mathbf{x} 's for repeated satellite overpasses, we can also derive the distribution of the bias over repeated \mathbf{x} realizations. In our particular case, we have $\text{bias}(\hat{\theta}) \sim \mathcal{N}(0.5714, 0.0533)$. This distribution is illustrated in

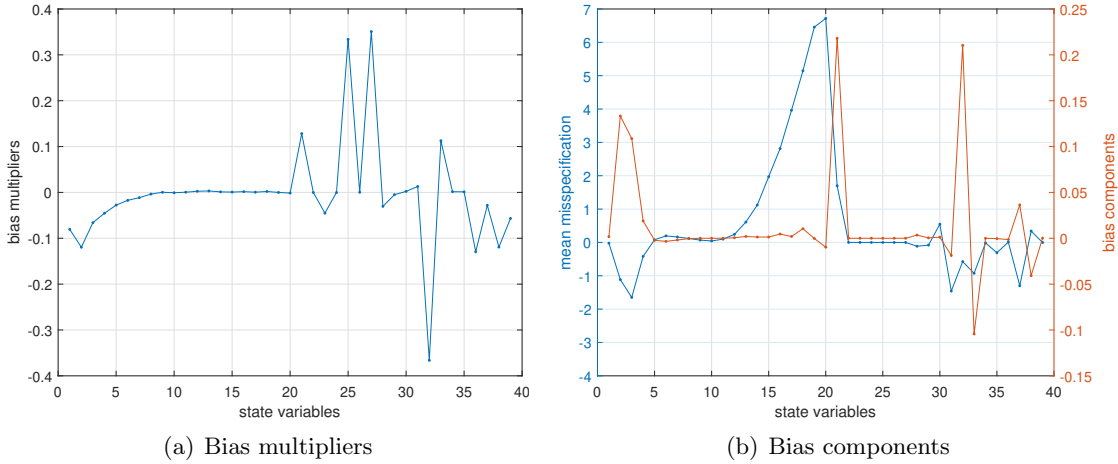


Figure 6. Figure (a) illustrates the bias multiplier vector \mathbf{m} , while Figure (b) shows the corresponding bias components $m_i(\mu_{\mathbf{x},i} - \mu_{a,i})$ for the misspecified means.

Figure 7(a) showing the bias for 10 000 instances of \mathbf{x} from the generative model. This shows that the biases are typically positive with a fair amount of spread around the central value. Negative biases and biases larger than 1.2 ppm are rare, at least in this particular setup for the retrieval problem.

We have that $\mathbb{E}_{\mathbf{x}}[\text{bias}(\hat{\theta})] = \mathbf{m}^T(\boldsymbol{\mu}_{\mathbf{x}} - \boldsymbol{\mu}_a)$, which corresponds to the bias expressions given in [28]. Hence, the distribution of $\text{bias}(\hat{\theta})$ has mean zero if and only if $\boldsymbol{\mu}_a = \boldsymbol{\mu}_{\mathbf{x}}$ or if $\boldsymbol{\mu}_{\mathbf{x}} - \boldsymbol{\mu}_a$ is orthogonal to \mathbf{m} . Even in those cases, $\text{bias}(\hat{\theta})$ would still have a spread around zero so that individual retrievals may be positively or negatively biased. In the more realistic case where $\mathbf{m}^T(\boldsymbol{\mu}_{\mathbf{x}} - \boldsymbol{\mu}_a) \neq 0$, the biases are either predominantly positive or negative depending on the details of the prior misspecification. Figure 6(b) shows a breakdown of the contribution of each state variable to the mean bias of 0.5714 in our particular setup. The figure visualizes the mean misspecification $\boldsymbol{\mu}_{\mathbf{x}} - \boldsymbol{\mu}_a$ and the individual terms $m_i(\mu_{\mathbf{x},i} - \mu_{a,i})$ contributing to the mean bias. It enables us to conclude that the positive biases are primarily caused by the misspecification of the surface pressure variable x_{21} , the aerosol variable x_{32} and the upper portion of the CO₂ profile, all of which contribute positively to the mean bias. The large misspecification of the lower portion of the CO₂ profile, on the other hand, makes negligible contribution to the bias due to the small bias multipliers of those variables.

5.2.2. Coverage and length of the operational and proposed intervals. The frequentist coverage of the operational method for a particular \mathbf{x} defined as $\mathbb{P}_{\varepsilon}(\theta \in [\underline{\theta}, \bar{\theta}])$ can be calculated using Equation (3.7). The coverage depends on \mathbf{x} only through $\text{bias}(\hat{\theta})$. To understand the nature of this dependence, we plot in Figure 7(a) the coverage of 95% intervals as a function of the bias for our particular retrieval setup. We observe that for $|\text{bias}(\hat{\theta})| < 0.84$ ppm the intervals overcover, while for $|\text{bias}(\hat{\theta})| > 0.84$ ppm the intervals undercover, with the coverage dropping sharply for biases larger than 1 ppm in absolute value. Since our biases are predominantly positive (Figure 7(a)), we are mostly going to observe the subrange of coverages corresponding to $\text{bias}(\hat{\theta}) \in [-0.3 \text{ ppm}, 1.4 \text{ ppm}]$.

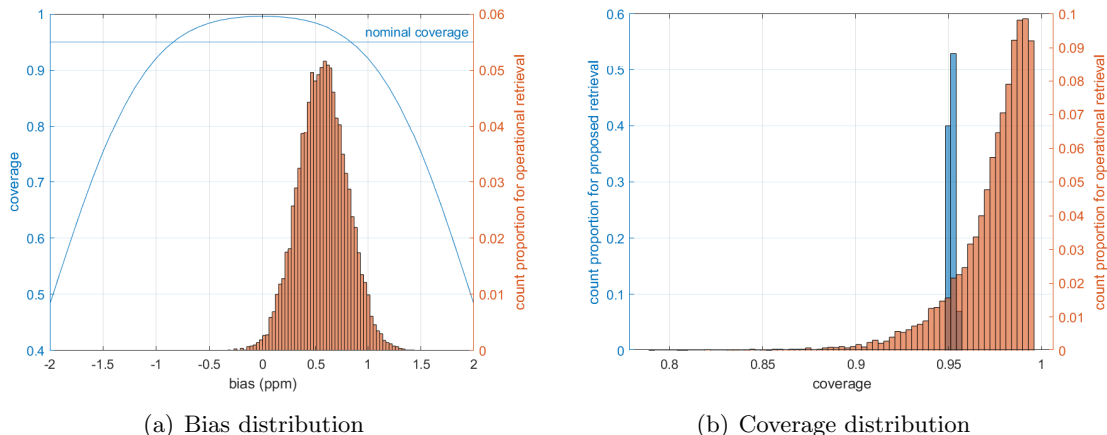


Figure 7. Figure (a) shows the coverage as a function of bias (blue line) for the operational procedure and the corresponding histogram of operational retrieval bias. Figure (b) shows a histogram (in orange color) of the operational retrieval coverage for 95% intervals. Also shown is a histogram (in blue color) of empirical coverage for the proposed frequentist uncertainty quantification method.

It is difficult to explicitly write down the distribution of the coverage corresponding to the assumed distribution of \mathbf{x} , but we evaluate the coverage distribution numerically in Figure 7(b) for 10000 state vectors and 95% intervals. We see that the operational intervals are poorly calibrated. For most \mathbf{x} realizations, the intervals have overcoverage. However, we also note that the coverage distribution is heavily left-skewed toward values below the nominal 95% coverage. In particular, for 12.03% of the \mathbf{x} realizations, the intervals have undercoverage. The smallest coverage is 79.0%, and this could drop even lower depending on the \mathbf{x} realization.

Such coverage behavior is inherent to the operational retrieval method because of the bias induced by the prior. This leads to the somewhat paradoxical conclusion that for most \mathbf{x} 's the operational intervals are too long, while for roughly 12% of the \mathbf{x} 's, the intervals are too short. The problem is that there is no easy way of telling when the intervals are too long or when they are too short, so it is not possible to adaptively recalibrate the interval lengths. One might also try to inflate all the interval lengths by some correction factor to mitigate the undercoverage tail, but this would shift the coverage distribution further to the right and the procedure would have even higher overcoverage. The appropriate correction factor would also depend on the unknown distribution of \mathbf{x} and could be very large.

The proposed frequentist direct retrieval method, on the other hand, has fundamentally different behavior in terms of the coverage. For this method, it is not straightforward to write down a closed-form expression for the coverage, but we can nevertheless evaluate it empirically. Here we evaluate the empirical coverage of 95% intervals using 10000 realizations of the noise ε . This is repeated for 100 realizations of \mathbf{x} from the generative distribution to study the distribution of the coverage values. The results are shown in Figure 7(b). We find that the proposed method is well-calibrated across all considered \mathbf{x} instances. The coverage peaks at slightly above 95%, with very little spread around that value. For some \mathbf{x} , the intervals have a small amount of overcoverage, but this is very minor in comparison to the

Table 2

Comparison of coverage and interval length (in ppm) between the operational and proposed uncertainty quantification methods for 10 state vector \mathbf{x} realizations chosen uniformly between the minimum and maximum coverage for the operational method in Figure 7(b). The target coverage in each case is 95%. Also shown are the bias of the operational point estimates and the standard deviation of the length of the proposed intervals (both in ppm).

\mathbf{x} realization	operational bias	operational coverage	operational length	proposed coverage	proposed avg. length	proposed length s.d.
1	1.4173	0.7899	3.94	0.9515	11.20	0.29
2	1.3707	0.8090	3.94	0.9511	11.20	0.28
3	1.2986	0.8363	3.94	0.9510	11.20	0.29
4	1.2357	0.8579	3.94	0.9515	11.20	0.28
5	1.1590	0.8816	3.94	0.9513	11.20	0.28
6	1.0747	0.9042	3.94	0.9512	11.21	0.27
7	0.9721	0.9272	3.94	0.9515	11.20	0.29
8	0.8420	0.9500	3.94	0.9513	11.19	0.31
9	0.6477	0.9730	3.94	0.9508	11.19	0.32
10	0.0001	0.9959	3.94	0.9502	11.18	0.35

operational method.

To further compare the two methods, we pick 10 instances of \mathbf{x} corresponding to 10 different coverage values for the operational method ranging from the minimum operational coverage to the maximum in Figure 7(b). Table 2 compares the 95% confidence intervals for the two methods for each of these 10 state vectors. We observe that while the coverage of the operational method can vary between drastic undercoverage and substantial overcoverage, the proposed method consistently achieves nearly nominal coverage irrespective of the \mathbf{x} realization.

The two approaches also have fundamentally different behaviors in terms of their interval lengths. The operational intervals have constant length $2z_{1-\alpha/2}\sigma$, where σ^2 is the posterior variance of θ that does not depend on the data \mathbf{y} , the noise ε or the state \mathbf{x} . In our case, $\sigma = 1.0051$ ppm, so the operational intervals have constant length of 3.94 ppm at 95% confidence level. It is worth noting that $\text{se}(\hat{\theta}) = 0.6856$ ppm. Hence the operational intervals derived from the posterior of θ are almost 50% longer than what the standard error intervals would be. This extra length gives the operational intervals some, but not enough, protection against undercoverage.

The proposed intervals, on the other hand, have data-dependent length. We report in Table 2 the average lengths and length standard deviations for these intervals across different noise ε realizations for each fixed state vector \mathbf{x} . We observe that the interval lengths indeed do vary across noise realizations for a given state vector with a coefficient of variation (ratio of standard deviation to average length) of about 3%. However, the average lengths are almost constant across different \mathbf{x} 's. We therefore conclude that, while the proposed intervals have variable length, their average length does not seem to depend much on the true state \mathbf{x} . Indeed, the average length of all the intervals forming the blue histogram in Figure 7(b) is

11.20 ppm, consistent with the individual values in Table 2.

The proposed intervals are longer than the operational ones, but in exchange appear to guarantee the desired coverage irrespective of the \boldsymbol{x} realization. In Section 6, we consider various ways of using additional constraints to reduce the interval length while maintaining nominal coverage. See also Section 7 for further discussion on the merits and limitations of the two approaches.

5.2.3. Illustrative instances. We pick some illustrative realizations to visualize the state vectors and confidence intervals produced by the two methods. We choose three representative cases corresponding to the minimum, nominal and maximum coverage for the operational method in Figure 7(b) which are also rows 1, 8 and 10 in Table 2, respectively.

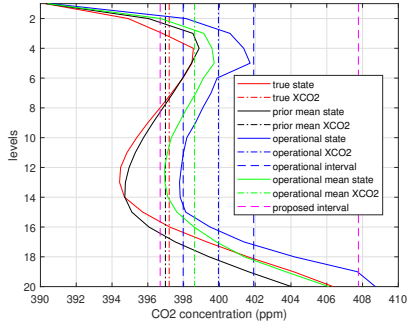
Figure 8(a) shows the CO₂ part of the \boldsymbol{x} instance having the smallest operational coverage. We observe, consistent with Section 5.2.1, that the operational interval is biased upward. It is overoptimistic about the amount of uncertainty, leading it to miss the true X_{CO_2} value for this particular $\boldsymbol{\varepsilon}$ realization. From Table 2, we know that this happens for roughly 21% of $\boldsymbol{\varepsilon}$ realizations when the noncoverage probability should ideally be only 5%. The proposed interval, on the other hand, is wider and as a result ends up covering the true X_{CO_2} value for the same \boldsymbol{x} and $\boldsymbol{\varepsilon}$ realizations. From Table 2, we know that the noncoverage probability for this interval is 5%, as it should be.

It is quite insightful to investigate the source of the upward bias for this \boldsymbol{x} realization. Contrary to what one might at first imagine, it is not caused by a misspecification of the CO₂ profile in the prior. In fact, as shown in Figure 8(a), the prior CO₂ profile is very similar to the true CO₂ profile in \boldsymbol{x} and the X_{CO_2} value implied by the prior is almost the same as the true X_{CO_2} value. Instead, it turns out that the bias is primarily caused by an upward fluctuation in the surface pressure variable x_{21} , as shown by Figure 8(b). The large positive difference in x_{21} between the true state and the prior gets multiplied by the relatively large positive bias multiplier of this variable (Figure 6(a); see also Section 5.2.1) leading to a large positive contribution to the overall bias. This results in a positively biased operational X_{CO_2} point estimate and a miscalibrated confidence interval.

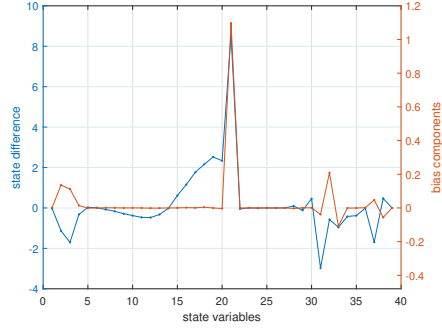
Next, instead of picking an adversarial \boldsymbol{x} , Figure 9(a) shows the \boldsymbol{x} realization corresponding to the largest coverage for the operational method. For this \boldsymbol{x} , the operational X_{CO_2} estimate is effectively unbiased and the operational interval covers the true X_{CO_2} value for almost all $\boldsymbol{\varepsilon}$ realizations, resulting in substantial overcoverage. The proposed interval, on the other hand, again has the desired 95% coverage, as indicated by Table 2. For the $\boldsymbol{\varepsilon}$ realization shown in the figure, the operational and proposed intervals both cover the true X_{CO_2} value.

Interestingly, the operational X_{CO_2} estimator in Figure 9(a) is effectively unbiased even though the prior is badly misspecified for this CO₂ profile. Figure 9(b) explains this phenomenon. Due to the small bias multipliers of the low-altitude CO₂ values (Figure 6(a)), prior misspecification in the lower half of the CO₂ profile creates little bias, while the misspecification in the upper half of the profile is such that it creates both positive and negative contributions to the bias that cancel out. At the same time, there is a consistent positive contribution to the bias from x_{32} , which is negated by a downward fluctuation in the pressure variable x_{21} and a consistent negative bias contribution from x_{33} .

Finally, we compare in Figure 10(a) the intervals for the \boldsymbol{x} realization that gives nominal

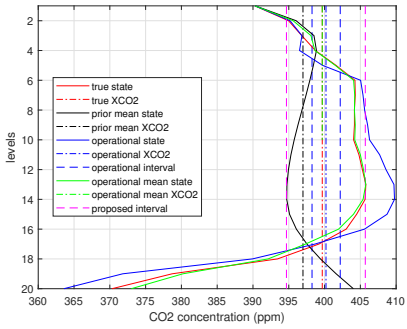


(a) Profile comparisons

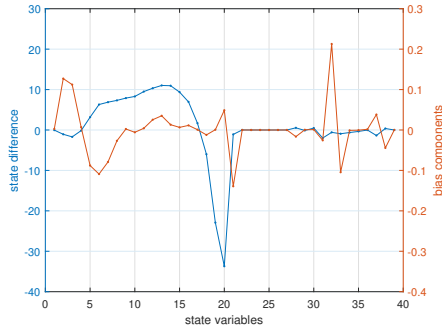


(b) Bias components

Figure 8. Figure (a) illustrates the operational and proposed intervals for the state realization that has the smallest coverage in Figure 7(b). Figure (b) visualizes the corresponding state differences $x_i - \mu_{a,i}$ and bias components $m_i(x_i - \mu_{a,i})$, where m_i is the i th bias multiplier.

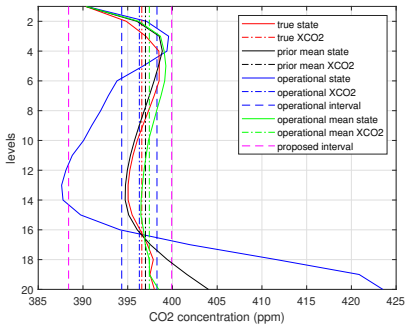


(a) Profile comparisons

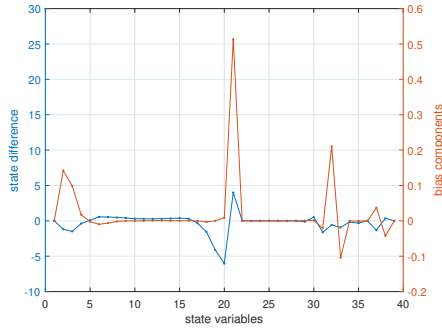


(b) Bias components

Figure 9. Figure (a) illustrates the operational and proposed intervals for the state realization that has the largest coverage in Figure 7(b). Figure (b) visualizes the corresponding state differences $x_i - \mu_{a,i}$ and bias components $m_i(x_i - \mu_{a,i})$, where m_i is the i th bias multiplier.



(a) Profile comparisons



(b) Bias components

Figure 10. Figure (a) illustrates the operational and proposed intervals for a state realization that has nominal coverage in Figure 7(b). Figure (b) visualizes the corresponding state differences $x_i - \mu_{a,i}$ and bias components $m_i(x_i - \mu_{a,i})$, where m_i is the i th bias multiplier.

coverage for the operational method in Table 2. For this \mathbf{x} , both intervals cover the true X_{CO_2} value for 95% of ε realizations. The ε realization shown in the figure has both intervals covering the true X_{CO_2} value. The operationally retrieved CO_2 profile has fluctuated quite substantially, but the anticorrelated fluctuations cancel out to produce a well-behaved confidence interval for X_{CO_2} . Overall, the operational method is slightly positively biased for X_{CO_2} , as expected based on the discussion in Section 5.2.2. Figure 10(b) reveals that the source of this bias is similar to the situation in Figure 8 in that the bias is primarily caused by the pressure variable x_{21} , albeit with a smaller magnitude. As before, the prior misspecification for the CO_2 profile near the surface (levels 18, 19 and 20) causes little harm due to the small bias multipliers of those variables (Figure 6(a)).

Overall, Figures 8–10 show how challenging it is to understand, predict and explain the uncertainty quantification performance of the operational retrieval method. The method can exhibit the very counterintuitive behavior where a relatively well-specified prior CO_2 profile (Figure 8) in fact has the worst coverage performance, while a badly misspecified prior CO_2 profile (Figure 9) has the highest coverage. The key to understanding the performance of the method, it turns out, is to understand the effect of the nuisance variables and how they interact with the misspecification of the CO_2 profile. Such analysis is obviously only possible when the true \mathbf{x} is known, which would make it very difficult to perform a similar study for real-life operational retrievals. The proposed method, on the other hand, is free from these complications and exhibits consistent 95% coverage for all \mathbf{x} realizations we have investigated.

5.3. Coverage over a spatial region. In this section, we investigate the performance of the operational method over the spatial grid of 8×8 soundings shown in Figure 5(a). The size of this region is approximately 8 km in the cross-track direction and 16 km in the along-track direction. We generate spatially correlated state vectors $\mathbf{x}(\mathbf{s}_i)$ and expected radiances $\mathbf{K}\mathbf{x}(\mathbf{s}_i)$ over the grid as described in Section 5.1.2. We then investigate the bias of the operational point estimates and the pointwise coverage of the operational 95% intervals over the grid. To do this, we can simply use the closed-form expressions (3.6) and (3.7) at each sounding location. Since both the bias and the coverage of the operational method are functions of the state vectors $\mathbf{x}(\mathbf{s}_i)$, these properties inherit the spatial dependence between the state vectors and will hence exhibit spatially correlated patterns.

We investigate in detail two $\{\mathbf{x}(\mathbf{s}_i) : i = 1, \dots, 64\}$ realizations over the grid: one that has a mixed pattern of both under- and overcoverage and another that has undercoverage for the entire grid. Figure 11(a) shows the coverage pattern for the first case, in which the coverage systematically changes from overcoverage to undercoverage when moving from the northwest corner of the grid to the southeast corner. The reason for this can be seen from the bias pattern in Figure 11(b) which shows that the overall positive bias has a systematic gradient across the region so that the bias is larger in the southeast corner and smaller in the northwest corner. Figure 12(a) shows the coverage pattern for the second case where the state vector realizations are such that all 64 intervals across the region have coverage below the nominal value. This is caused by a systematic large positive bias throughout the region as shown in Figure 12(b).

These results illustrate one of the drawbacks of the operational retrieval in that there can be entire regions with undercoverage or overcoverage. For example, in the case of Figure 12,

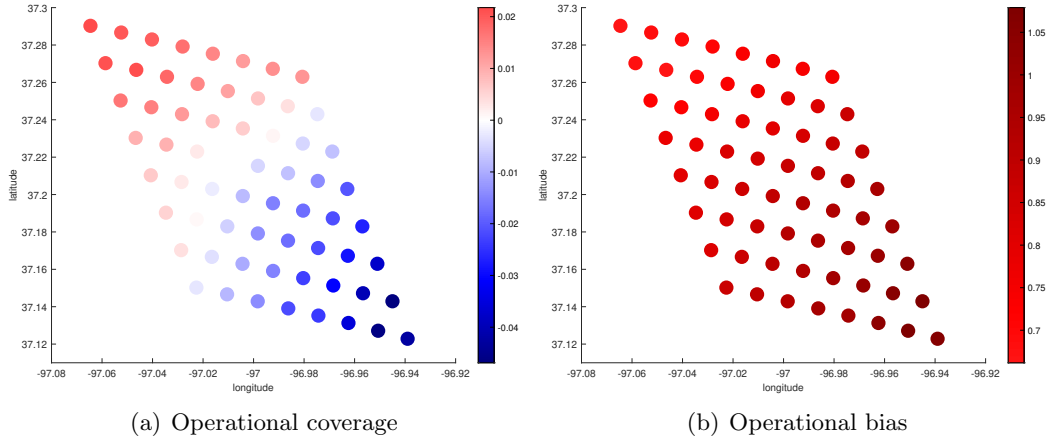


Figure 11. Operational retrieval over a grid of 8×8 soundings for an instance where both undercoverage and overcoverage are present. Figure (a) shows the spatial coverage pattern relative to the nominal 95% in units of probability (i.e., -0.03 , for example, corresponds to coverage 0.92 , instead of the nominal 0.95). The fraction of soundings below nominal coverage is 0.55 . Figure (b) shows the corresponding bias pattern in ppm.

all intervals across the region are systematically too high which causes their lower bounds to miss the corresponding true X_{CO_2} values more often than they should. There is a risk that such patterns could be mistaken as CO_2 flux signals. As such, these observations may have important implications for carbon flux estimates, as discussed later in Section 7.

The coverage patterns shown here for the operational method are in stark contrast with the behavior of the proposed frequentist method which does not exhibit systematic spatially correlated miscalibration. There is also little hope of correcting the situation with the operational method. If we, for example, tried to systematically increase the interval length in Figure 11 to correct for the undercoverage, we would observe higher overcoverage for some of the other soundings. Worse still, without access to the unknown true state vectors, it is very difficult to tell if a given region has well-calibrated uncertainties or whether all or some of the intervals have systematic under- or overcoverage.

6. Variable importance and effect of additional constraints on interval length. As demonstrated in the previous section, the proposed frequentist method has good coverage performance, but the intervals are longer in comparison to the existing operational retrieval method. In this section, we consider different variants of the proposed method to improve the interval length.

It is worth noting that the underlying inference problem is defined by (i) the forward operator, which in the linearized approximation is simply the forward matrix \mathbf{K} , (ii) the functional of interest, which for linear functionals is parameterized by the weight vector \mathbf{h} , (iii) the amount of noise in the problem, which is controlled by the covariance Σ_ϵ given the Gaussian noise approximation, and (iv) the constraint set C . For a given sounding and quantity of interest, we cannot change \mathbf{K} , Σ_ϵ or \mathbf{h} , but we can potentially alter C . In this section, we therefore investigate how changes in C in the form of additional constraints affect the length of the proposed intervals.

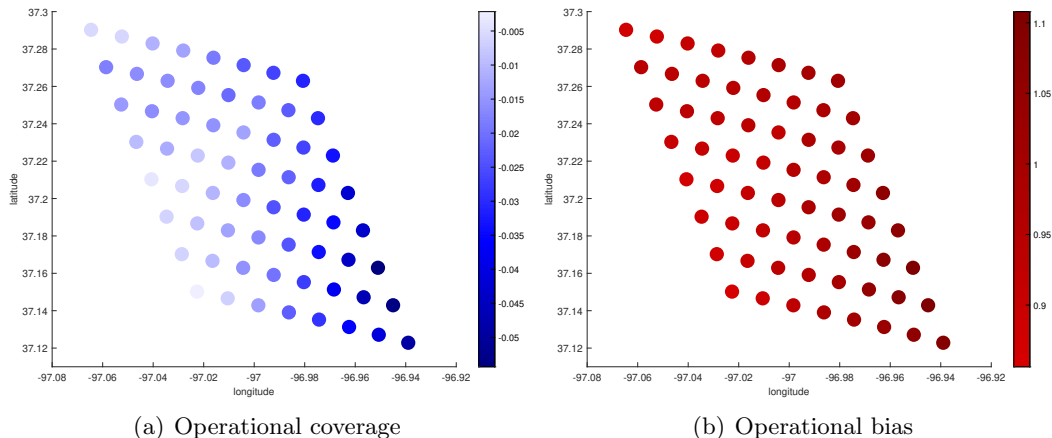


Figure 12. Operational retrieval over a grid of 8×8 soundings for an instance with undercoverage for the entire grid. Panels (a) and (b) are as in Figure 11.

6.1. Motivation. So far, we have only used trivial positivity constraints on certain state vector elements; see Section 5.1.4. However, if additional information was available to further constrain the state vector, then including those constraints would result in shorter intervals for X_{CO_2} . For example, one could imagine that observational data from other sources tell us that $x_i \in [\underline{x}_i, \bar{x}_i]$ with a high probability for some x_i in the state vector. To investigate what impact this would have, we start by considering how each variable in the retrieval problem affects the final interval length. We then provide a framework for incorporating this kind of additional probabilistic information while still maintaining finite-sample coverage for X_{CO_2} .

6.2. Effect of individual nuisance variables. We first consider the effect of each nuisance variable x_{21}, \dots, x_{39} on the X_{CO_2} interval length. Figure 13(a) shows the average interval lengths for the proposed method when one of the nuisance variables is assumed to be known. We can incorporate this assumption by using constraints of the form $x_{i,\text{true}} \leq x_i \leq x_{i,\text{true}}$ for one x_i at a time, in addition to the previously used positivity constraints. As expected, the interval lengths are smaller than the interval length without any additional information which is shown by the red horizontal bar. In particular, variables x_{21} (surface pressure) and x_{28} (log-AOD for the first composite aerosol type) have the greatest impact on the interval length. Therefore additional constraints on these two variables could be particularly helpful in reducing the interval length. Since it is not immediately clear what observational constraints might be available for the specific aerosol type corresponding to x_{28} , we will in the following focus on constraints for the pressure variable x_{21} .

6.3. Deterministic pressure constraints. We analyze the effect of various degrees of deterministic constraints on the pressure variable in Figure 13(b). Instead of assuming that the pressure is known exactly as was done in Figure 13(a), we consider symmetric constraints about the true pressure value, i.e., constraints of the form $x_{21,\text{true}} - \delta \leq x_{21} \leq x_{21,\text{true}} + \delta$ for various δ . As expected, we observe that tighter constraints on pressure translate into shorter intervals for X_{CO_2} . For example, knowing the pressure to within ± 3 hPa lets us decrease the

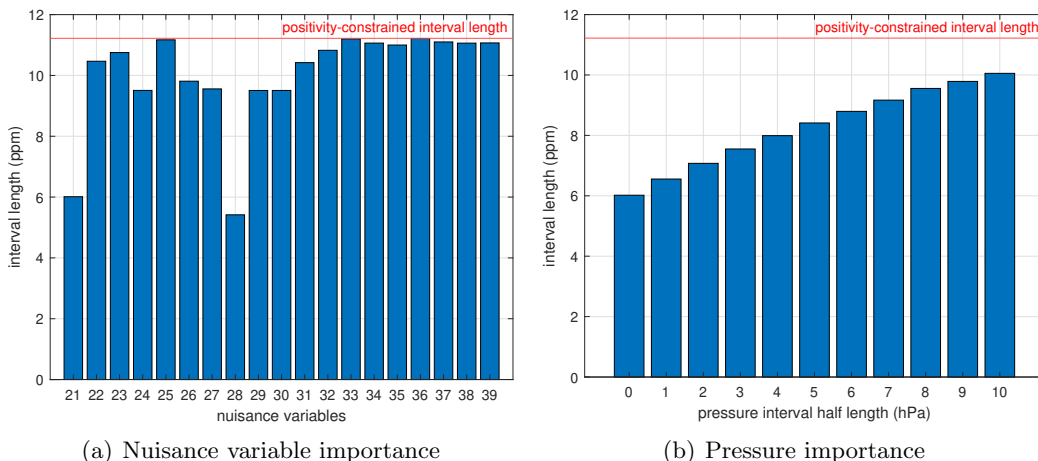


Figure 13. Figure (a) shows average X_{CO_2} interval lengths at 95% confidence level when fixing one nuisance variable at a time to its true value. The horizontal red line is the interval length when none of the variables are fixed and only trivial positivity constraints are used. Figure (b) shows average X_{CO_2} interval lengths at 95% confidence level for varying degrees of deterministic constraints on the surface pressure variable x_{21} . The horizontal red line again shows the interval length when only the positivity constraint is used.

average X_{CO_2} interval length from 11.19 ppm to 7.55 ppm. Knowing the surface pressure to within such, or even higher, accuracy is not impossible as there are other, complementary observing systems (such as ground-based weather stations) that are capable of providing pressure information within such limits.

We remark that the interval lengths in Figures 13(a) and 13(b) are averages over 100 noise realizations for the \mathbf{x} realization corresponding to nominal operational coverage in Table 2; see also Figure 10. We have also studied other \mathbf{x} 's from the generative model and found qualitatively similar results.

6.4. Probabilistic constraints and interval length optimization. In the previous section, we analyzed the effect of additional deterministic constraints on pressure. However, such constraints might not always be available with full certainty, but we might instead know that they hold with a high probability. This is the case, for example, when a frequentist confidence interval is available from another observing system. In this section, we show how to incorporate such probabilistic constraints within the proposed framework to reduce the final interval length.

6.4.1. Coverage calibration. To explain the key idea, imagine that instead of having deterministic constraints such as $x_{i,\text{true}} - \delta \leq x_i \leq x_{i,\text{true}} + \delta$, we have confidence intervals for one or more of the x_i 's such that $\underline{x}_i(\alpha_i) \leq x_i \leq \overline{x}_i(\alpha_i)$ with frequentist coverage at least $(1 - \alpha_i)$, i.e., $\mathbb{P}(x_i \in [\underline{x}_i(\alpha_i), \overline{x}_i(\alpha_i)]) \geq 1 - \alpha_i$. We can then construct a $(1 - \alpha)$ confidence interval for the quantity of interest θ by running the proposed retrieval procedure with these probabilistic constraints at an internal confidence level $(1 - \gamma)$ chosen so that, accounting for the α_i 's, we can still maintain the required nominal coverage. One way to adjust γ is to bound

the error probabilities as follows:

$$\begin{aligned}
\mathbb{P}(\theta \notin [\underline{\theta}, \bar{\theta}]) &= \mathbb{P}(\theta \notin [\underline{\theta}, \bar{\theta}], x_i \in [\underline{x}_i(\alpha_i), \bar{x}_i(\alpha_i)] \text{ for all } i) \\
&\quad + \mathbb{P}(\theta \notin [\underline{\theta}, \bar{\theta}], x_i \notin [\underline{x}_i(\alpha_i), \bar{x}_i(\alpha_i)] \text{ for some } i) \\
&= \mathbb{P}(\theta \notin [\underline{\theta}, \bar{\theta}] \mid x_i \in [\underline{x}_i(\alpha_i), \bar{x}_i(\alpha_i)] \text{ for all } i) \cdot \mathbb{P}(x_i \in [\underline{x}_i(\alpha_i), \bar{x}_i(\alpha_i)] \text{ for all } i) \\
&\quad + \mathbb{P}(\theta \notin [\underline{\theta}, \bar{\theta}], x_i \notin [\underline{x}_i(\alpha_i), \bar{x}_i(\alpha_i)] \text{ for some } i) \\
&\leq \mathbb{P}(\theta \notin [\underline{\theta}, \bar{\theta}] \mid x_i \in [\underline{x}_i(\alpha_i), \bar{x}_i(\alpha_i)] \text{ for all } i) \\
&\quad + \mathbb{P}(x_i \notin [\underline{x}_i(\alpha_i), \bar{x}_i(\alpha_i)] \text{ for some } i) \\
&\leq \mathbb{P}(\theta \notin [\underline{\theta}, \bar{\theta}] \mid x_i \in [\underline{x}_i(\alpha_i), \bar{x}_i(\alpha_i)] \text{ for all } i) \\
&\quad + \sum_i \mathbb{P}(x_i \notin [\underline{x}_i(\alpha_i), \bar{x}_i(\alpha_i)]) \\
(6.1) \quad &\leq \gamma + \sum_i \alpha_i,
\end{aligned}$$

where i ranges over those variables that have probabilistic constraints. Thus, if we choose γ and the α_i 's in such a way that $\gamma + \sum_i \alpha_i = \alpha$, then we can keep the desired $(1 - \alpha)$ coverage for the interval $[\underline{\theta}, \bar{\theta}]$. Notice the similarity of this construction to the Bonferroni method in multiple testing (see, e.g., Section 10.7 in [47]).

6.4.2. Demonstration with pressure intervals. Since in our case adding deterministic constraints on the pressure variable x_{21} provides a gain in the interval length, we now analyze the effect of probabilistic constraints on that variable. This demonstrates the simplest application of Equation (6.1) in a case where there is a probabilistic constraint on a single variable only. We therefore need to choose γ and α_{21} such that $\gamma + \alpha_{21} = \alpha$, where we set $\alpha = 0.05$ to obtain a 95% final interval for X_{CO_2} . By Equation (6.1), any positive γ and α_{21} summing to 0.05 will give a valid final interval, but an optimal choice is such that it minimizes the final interval length. To start investigating the dependence of the X_{CO_2} interval length on these choices, Figure 14(a) shows how the length the pressure interval and the confidence level $(1 - \gamma)$ of the X_{CO_2} interval jointly affect the average X_{CO_2} interval length. Using Figure 14(a), we can set the internal confidence level $(1 - \gamma)$ to a value larger than 95% to account for the coverage probability $(1 - \alpha_{21})$ of the pressure interval. To optimize this choice, we need to relate α_{21} to the length of the pressure interval. In this study, we assume that there is a pressure sensor that provides pressure observations \hat{x}_{21} following the Gaussian distribution $\mathcal{N}(x_{21}, \sigma_{21}^2)$. We then assume that the pressure intervals are $(1 - \alpha_{21})$ standard error intervals of length $2z_{1-\alpha_{21}/2}\sigma_{21}$, where σ_{21} is the pressure standard error.

For a given σ_{21} , we can then trace through Figure 14(a) for various γ and the corresponding α_{21} and record the final X_{CO_2} interval length. Figure 14(b) shows examples of this for pressure standard errors σ_{21} ranging from 0.5 hPa to 4 hPa. Each curve represents the average interval length for the proposed method for different γ and can be used to choose γ such that the final interval length is optimized. Along each curve, we have indicated this optimal internal confidence level. We observe that for moderate values of the pressure standard error, the optimal internal confidence level is greater than 95%, but when the pressure standard error is either very small or very large, the optimal internal confidence level approaches 95%. This is

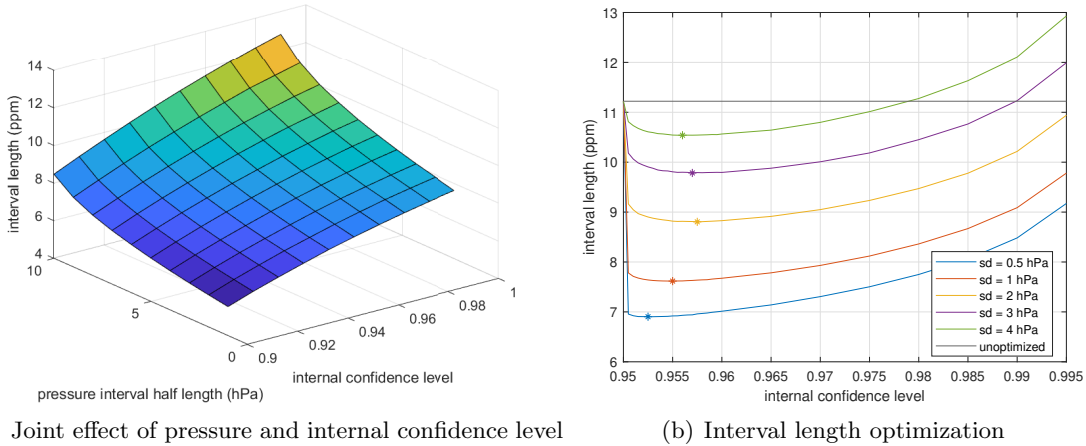


Figure 14. Figure (a) shows the joint effect of pressure interval length and internal confidence level on the average X_{CO_2} interval length. Figure (b) shows the optimization of the average X_{CO_2} interval length for various pressure standard errors by trading off the internal confidence level ($1 - \gamma$) for the confidence level of the pressure interval ($1 - \alpha_{21}$). The values that optimize the interval length are marked with asterisks.

because when the pressure standard error is very small, it is almost as good as using the correct value of the pressure variable, while when the standard error is very large, it is almost as good as not using any additional constraints on the pressure variable besides the non-negativity constraint.

Since the proposed interval has variable, data-dependent length, there is an important subtlety in that the above interval length optimization must be done without using the observed data \mathbf{y} so as to guarantee the coverage in Equation (6.1). In addition, we would ideally like to optimize the average interval length which cannot be done based on a single \mathbf{y} . We therefore need a candidate state vector \mathbf{x} that can be used to calculate average interval lengths which can then be used as the basis for the length optimization. Since we found in Section 5 that the average interval lengths are not very sensitive to the choice of \mathbf{x} , it suffices to have a reasonable ansatz of what \mathbf{x} might look like. Luckily, we already have that in the prior mean $\boldsymbol{\mu}_a$ of the operational method. In this study, we therefore set the state vector \mathbf{x} equal to $\boldsymbol{\mu}_a$ for the interval length optimization. The interval lengths shown in Figures 14(a) and 14(b) were then obtained as averages over 100 noise realizations for this choice of \mathbf{x} and for pressure intervals centered at $x_{21} = \mu_{a,21}$.

We now proceed to empirically verify the coverage of the final intervals constructed as described above. The length optimization phase can be run based on $\boldsymbol{\mu}_a$ and σ_{21} and before seeing \mathbf{y} . This leads to an optimal choice of γ and α_{21} irrespective of \mathbf{y} , and, fixing these values, one can then check the coverage and length of the intervals for multiple \mathbf{y} realizations corresponding to a fixed \mathbf{x} . We use the \mathbf{x} that provides nominal coverage for the operational retrieval method in Table 2 as the state vector for this evaluation. While the length optimization was done without fluctuating the pressure intervals, the coverage study also accounts for the variation of the pressure intervals by simulating intervals of the form $[\hat{x}_{21} - z_{1-\alpha_{21}/2}\sigma_{21}, \hat{x}_{21} + z_{1-\alpha_{21}/2}\sigma_{21}]$ for the optimized α_{21} and for $\hat{x}_{21} \sim \mathcal{N}(x_{21}, \sigma_{21}^2)$ inde-

Table 3

Optimized confidence levels, final empirical coverage and average length for the X_{CO_2} intervals incorporating probabilistic pressure constraints at various levels of pressure standard error. The internal and pressure confidence levels are chosen so that the final interval has at least 95% coverage.

pressure std. err. (hPa)	internal conf. level ($1 - \gamma$)	pressure conf. level ($1 - \alpha_{21}$)	final empirical coverage	interval length (ppm)
0.5	0.9525	0.9975	0.9741	6.89
1	0.9550	0.9950	0.9782	7.61
2	0.9575	0.9925	0.9743	8.80
3	0.9570	0.9930	0.9684	9.71
4	0.9560	0.9940	0.9629	10.32

pendently of ε . The results are given in Table 3 which shows the optimized confidence levels ($1 - \gamma$) and ($1 - \alpha_{21}$) as well as the empirical coverage and average length of the final X_{CO_2} intervals based on 10 000 realizations. We observe that the intervals maintain the 95% coverage guarantee while significantly reducing the final interval length. The amount of gain provided by the pressure information depends on the level of uncertainty in the pressure intervals. In particular, for pressure standard error of 0.5 hPa, we are able to reduce the average interval length to 6.89 ppm from the original 11.19 ppm. The final intervals are somewhat conservative due to the slack in the inequalities in Equation (6.1). Notice also that the interval lengths predicted by the prior-based optimization in Figure 14(b) match well with the final values in Table 3 even though this evaluation is for a different \mathbf{x} .

Finally, we note that this framework can be used to incorporate probabilistic constraints on multiple nuisance variables. In this case, using the union bound to control the miscoverage probability, as is done in the second last inequality in Equation (6.1), might be loose and additional structure among the probabilistic constraints, such as independence, could provide additional gain.

7. Conclusions and outlook. Our focus on the frequentist properties of the uncertainty estimates is one of the main differences between this work and much of the other related work on uncertainty quantification in remote sensing, which tends to predominantly focus on Bayesian approaches. The frequentist and Bayesian paradigms answer fundamentally different questions about the unknown parameter θ , and as is well known from the extensive debate in the literature, both approaches are valuable in their own right. The question we set out to answer is the following: Given a fixed state of the atmosphere corresponding to a given satellite overpass, what are the repeated sampling properties of the confidence intervals, where the repetitions are over the instrument noise ε ? Hence, most of our probabilities and expectations are taken with respect to the noise ε , while some previous works take expectations over both ε and \mathbf{x} [15, 28]. Arguably, properties calculated with respect to ε are more relevant for downstream scientific use, where, for example, carbon flux estimates use OCO-2 data to gain information about the instantaneous state of the atmosphere corresponding to a particular \mathbf{x} instead of an average \mathbf{x} .

To interpret the frequentist X_{CO_2} intervals, it is crucial to understand that the $(1 - \alpha)$ coverage property not only holds for a collection of intervals from a given sounding location, but also for a collection of intervals arising from soundings at different locations, since the noise ε is independent across soundings. Imagine a collection of, say, 10 000 sounding locations within an OCO-2 orbit, each with a realization of a 95% frequentist confidence interval for X_{CO_2} . Then, we know that roughly 9 500 of these intervals cover their true X_{CO_2} value, and the coverage/non-coverage pattern should not have any apparent spatial structure. It is foreseeable that such intervals could be used to produce rigorous uncertainties in downstream scientific tasks by, for example, using techniques similar to those described here for X_{CO_2} . Our grid sounding experiments show that the same conclusion, however, does not necessarily hold for the operational Bayesian retrievals. Let I_k be the indicator random variable indicating whether the k th interval covers its true X_{CO_2} value, where k ranges over the spatial sounding locations within the orbit. For properly calibrated frequentist intervals, the I_k 's are independent and identically distributed across the sounding locations, while in the case of the operational retrievals, the I_k 's are independent across the sounding locations, but no longer identically distributed. Instead, the coverage probability $\mathbb{P}_\varepsilon(I_k = 1)$ varies throughout the orbit in a systematic, spatially coherent way, so that in some parts of the orbit perhaps 85% of the intervals are expected to cover while in other parts maybe 99% of the intervals cover. Since there is no straightforward way of telling, based on OCO-2 data alone, which of these situations applies in a given region, it is not clear how to rigorously use such uncertainties in downstream scientific tasks.

An important question for future work is to understand what implications these conclusion have on CO_2 flux estimates. A key question concerns the spatial length scales at which the biases occur in operational X_{CO_2} point estimates and intervals. Our results indicate that there are spatially correlated biases at least at scales of 8×8 soundings (roughly $8 \text{ km} \times 16 \text{ km}$), which is likely to have implications for regional carbon flux estimates, for example, over urban areas. This conclusion is further corroborated by OCO-2's target mode observations taken on orbits near TCCON sites in order to assess the empirical behavior of OCO-2 retrievals for individual overpasses [50]. Indeed, the retrieval errors for a single target overpass have been found to exhibit substantial spatial correlation [51]. However, as of now, we do not know whether these bias patterns persist at the scale of a single pixel in global flux inversion models, where the grid resolution is typically of the order of a few hundred kilometers. Further studies are therefore required to understand if the observed biases persist at these scales. If they do, then it would be useful to understand how to incorporate our proposed intervals, which do not exhibit such spatially correlated biases, into global flux inversion models.

An important insight provided by this work is the identification of the surface pressure (x_{21}) and the AOD of the first composite aerosol type (x_{28}) as key variables affecting the length of the frequentist confidence intervals (Figure 13(a)). This raises the interesting possibility of obtaining more precise X_{CO_2} estimates by developing Level 2 retrieval methods that combine pressure or aerosol information from other satellites or observing systems with OCO-2 data. The surface pressure also plays an important role in explaining the performance of the operational Bayesian retrievals (Figures 8–10), which has also been noted in previous studies; see [20] and the references therein. Interestingly, x_{28} , on the other hand, does not particularly stand out in the analysis of the operational method. However, another aerosol

variable (x_{32}) is responsible for a consistent positive contribution to the bias due to its large bias multiplier (Figure 6(a)), moderately misspecified prior mean (Table 1) and very small generative process variance (Table 1). A more comprehensive analysis of the effects of the different variables, including at different spatial regions, seasons and observing modes, is left as a subject for future work.

In this paper, we have considered a linearized approximation of the nonlinear OCO-2 forward operator. A major topic for future work would be to extend this work to nonlinear forward operators. The basic primal approach from [37], outlined in Section 4.2.1, still applies in that the extremal values of $\mathbf{h}^T \mathbf{x}$ over $\mathbf{x} \in C \cap D$ would define valid $(1 - \alpha)$ simultaneous confidence intervals. What is not immediately clear, however, is whether the approach from [35, 36] for turning these into one-at-a-time intervals still applies. Another major challenge concerns the computation of the intervals since now D can no longer be described by a quadratic inequality and might even be non-convex, depending on the properties of the forward operator. Constructing and characterizing the dual problems would also be substantially more difficult. Nevertheless, since \mathbf{x} here has a moderate dimension, it is plausible that methods can be developed for solving the primal optimization problems within the time constraint requirements of the OCO-2 mission.

We have shown empirically that the proposed intervals consistently have frequentist coverage very close to the nominal value. In future work, we hope to be able to show what conditions are needed in order to rigorously guarantee this. As has been pointed out in [45], the previous proof in [36] appears to be incorrect. The authors in [45] even provide a counterexample showing that the intervals can undercover for \mathbf{h} containing both positive and negative elements. This leaves open the question of whether it is possible to guarantee the coverage when all elements of \mathbf{h} have the same sign, as is the case here with the X_{CO_2} functional. If it turns out to be difficult to provide such guarantees, it then becomes necessary to empirically analyze the performance of the intervals under various atmospheric states and OCO-2 observing scenarios to verify that the excellent performance observed here extends to those situations as well.

Another open question concerns the optimality of the intervals in terms of their length. While the proposed intervals have much better frequentist calibration, they are almost three times as long as the current operational intervals, when only trivial constraints are applied. Therefore, an important question for future work would be to understand what can be said about the optimality of the length of these intervals within the class of methods that provide frequentist coverage guarantees. Donoho introduced in [9] intervals that are up to a multiplicative factor minimax optimal for this problem among the class of fixed-length intervals with guaranteed coverage. The intervals studied here are variable-length and may hence be shorter than those of [9]. To the best of our knowledge, minimax optimality of variable-length intervals for this problem remains an open question. Furthermore, instead of minimax, a more appropriate notion of optimality here might be one with respect to a reasonable distribution on \mathbf{x} , such as the operational prior distribution.

Finally, it is important to highlight that the implicit regularization provided by the functional \mathbf{h} is a key reason the proposed method yields intervals with a reasonable length despite the ill-posedness of the problem. Some functionals are inherently easier to retrieve than others. Intuitively, aggregate quantities, such as X_{CO_2} , are easier to constrain than, for example,

CO₂ concentrations at individual pressure levels. Given that one of the main uses of OCO-2 data is in carbon flux inversions, it would be important to understand whether X_{CO_2} is the best functional for summarizing the information content in the radiances for the purpose of flux inversions. Namely, it could be that there are nearby functionals that can be retrieved with a higher accuracy while still containing almost the same amount of information about the fluxes. The singular value decomposition of the forward matrix \mathbf{K} can be used to obtain a rough idea about the difficulty of retrieving a given functional \mathbf{h} , but accounting for the effect of the constraints on \mathbf{x} would require a more sophisticated approach. More generally, it would be interesting to see if the interval construction could be customized for the chosen functional by, for example, adapting the data-space confidence set to the functional and the available constraints, as suggested in [37].

Appendix A. Computational simplification. Consider again the original problem in the primal form to obtain the lower endpoint $\underline{\theta}$:

$$(A.1) \quad \begin{aligned} & \text{minimize} && \mathbf{h}^T \mathbf{x} \\ & \text{subject to} && \|\mathbf{y} - \mathbf{K}\mathbf{x}\|^2 \leq z_{1-\alpha/2}^2 + s^2, \\ & && \mathbf{A}\mathbf{x} \leq \mathbf{b}, \end{aligned}$$

where $s^2 = \min_{\mathbf{x}: \mathbf{A}\mathbf{x} \leq \mathbf{b}} \|\mathbf{y} - \mathbf{K}\mathbf{x}\|^2$.

Let us consider the singular value decomposition $\mathbf{K} = \mathbf{U}\mathbf{D}\mathbf{V}^T$. We first note that $\|\mathbf{y} - \mathbf{K}\mathbf{x}\|^2 = \|\mathbf{U}^T\mathbf{y} - \mathbf{D}\mathbf{V}^T\mathbf{x}\|^2$, since $\mathbf{U}^T\mathbf{U} = \mathbf{U}\mathbf{U}^T = \mathbf{I}$. Further, as $n > p$, let us denote by $\tilde{\mathbf{y}}_{1:p}$ the first p entries of $\tilde{\mathbf{y}} = \mathbf{U}^T\mathbf{y}$ and by $\tilde{\mathbf{y}}_{p+1:n}$ the rest of the entries of $\tilde{\mathbf{y}}$. Then, we can write $\|\mathbf{U}^T\mathbf{y} - \mathbf{D}\mathbf{V}^T\mathbf{x}\|^2 = \|\tilde{\mathbf{y}}_{1:p} - \mathbf{D}_{1:p,:}\mathbf{V}^T\mathbf{x}\|^2 + \|\tilde{\mathbf{y}}_{p+1:n}\|^2$, where $\mathbf{D}_{1:p,:}$ denotes the first p rows of \mathbf{D} . This suggests a simplification of the primal problem where, instead of (A.1), we solve the following equivalent problem to obtain the lower endpoint $\underline{\theta}$:

$$(A.2) \quad \begin{aligned} & \text{minimize} && \mathbf{h}^T \mathbf{x} \\ & \text{subject to} && \|\tilde{\mathbf{y}}_{1:p} - \mathbf{D}_{1:p,:}\mathbf{V}^T\mathbf{x}\|^2 \leq z_{1-\alpha/2}^2 + \tilde{s}^2, \\ & && \mathbf{A}\mathbf{x} \leq \mathbf{b}, \end{aligned}$$

where now $\tilde{s}^2 = \min_{\mathbf{x}: \mathbf{A}\mathbf{x} \leq \mathbf{b}} \|\tilde{\mathbf{y}}_{1:p} - \mathbf{D}_{1:p,:}\mathbf{V}^T\mathbf{x}\|^2$. This is equivalent to the original problem because $s^2 = \tilde{s}^2 + \|\tilde{\mathbf{y}}_{p+1:n}\|^2$. When $n \gg p$, solving problem (A.2), including the associated slack problem, is much faster than solving problem (A.1), because the norms involve p -variate vectors instead of n -variate vectors. An analogous simplification can obviously be used with the upper endpoint $\bar{\theta}$ as well. These simplifications proved crucial for our ability to perform the empirical coverage studies presented in this paper.

Appendix B. Dual derivation. Consider the primal optimization problem to obtain the lower endpoint $\underline{\theta}$:

$$(B.1) \quad \begin{aligned} & \text{minimize} && \mathbf{h}^T \mathbf{x} \\ & \text{subject to} && \|\mathbf{y} - \mathbf{K}\mathbf{x}\|^2 \leq z_{1-\alpha/2}^2 + s^2, \\ & && \mathbf{A}\mathbf{x} \leq \mathbf{b}, \end{aligned}$$

where s^2 is the slack factor. For notational convenience, we let $z_{1-\alpha/2}^2 + s^2 = q^2$.

We first write an equivalent problem as follows:

$$(B.2) \quad \begin{aligned} & \text{minimize} && \mathbf{h}^T \mathbf{x} \\ & \text{subject to} && \mathbf{y} - \mathbf{K} \mathbf{x} = \mathbf{r}, \\ & && \|\mathbf{r}\|^2 \leq q^2, \\ & && \mathbf{A} \mathbf{x} \leq \mathbf{b}, \end{aligned}$$

where the optimization is now over both \mathbf{x} and \mathbf{r} .

The Lagrangian of the above problem can be written as

$$(B.3) \quad L(\mathbf{x}, \mathbf{r}, \mathbf{w}, \lambda, \mathbf{c}) = \mathbf{h}^T \mathbf{x} + \mathbf{w}^T (\mathbf{y} - \mathbf{K} \mathbf{x} - \mathbf{r}) + \lambda (\|\mathbf{r}\|^2 - q^2) + \mathbf{c}^T (\mathbf{A} \mathbf{x} - \mathbf{b}),$$

where \mathbf{w} , $\lambda \geq 0$ and $\mathbf{c} \geq \mathbf{0}$ are dual variables [3].

The dual function is obtained by minimizing the Lagrangian with respect to the primal variables \mathbf{x} and \mathbf{r} :

$$(B.4) \quad g(\mathbf{w}, \lambda, \mathbf{c}) = \inf_{\mathbf{x}, \mathbf{r}} L(\mathbf{x}, \mathbf{r}, \mathbf{w}, \lambda, \mathbf{c}).$$

We first rewrite the Lagrangian to group the terms corresponding to \mathbf{x} and \mathbf{r} together:

$$(B.5) \quad L(\mathbf{x}, \mathbf{r}, \mathbf{w}, \lambda, \mathbf{c}) = (\mathbf{h} - \mathbf{K}^T \mathbf{w} + \mathbf{A}^T \mathbf{c})^T \mathbf{x} - \mathbf{w}^T \mathbf{r} + \lambda \|\mathbf{r}\|^2 + \mathbf{w}^T \mathbf{y} - \lambda q^2 - \mathbf{c}^T \mathbf{b}.$$

Next, we note that we can restrict ourselves to the case where $\mathbf{h} - \mathbf{K}^T \mathbf{w} + \mathbf{A}^T \mathbf{c} = \mathbf{0}$, since otherwise the Lagrangian is unbounded below as a linear function in \mathbf{x} . By minimizing with respect to \mathbf{r} and substituting back, we obtain the dual function

$$(B.6) \quad g(\mathbf{w}, \lambda, \mathbf{c}) = -\frac{1}{4\lambda} \|\mathbf{w}\|^2 + \mathbf{w}^T \mathbf{y} - \lambda q^2 - \mathbf{c}^T \mathbf{b},$$

where $\mathbf{h} - \mathbf{K}^T \mathbf{w} + \mathbf{A}^T \mathbf{c} = \mathbf{0}$, $\lambda \geq 0$ and $\mathbf{c} \geq \mathbf{0}$. The dual optimization problem is then the problem of maximizing $g(\mathbf{w}, \lambda, \mathbf{c})$ with respect to the dual variables \mathbf{w} , λ and \mathbf{c} . Maximization with respect to λ can be carried out in closed form. We can thus eliminate λ to obtain the following dual problem for the remaining variables \mathbf{w} and \mathbf{c} :

$$(B.7) \quad \begin{aligned} & \text{maximize} && \mathbf{w}^T \mathbf{y} - \sqrt{z_{1-\alpha/2}^2 + s^2} \|\mathbf{w}\| - \mathbf{b}^T \mathbf{c} \\ & \text{subject to} && \mathbf{h} + \mathbf{A}^T \mathbf{c} - \mathbf{K}^T \mathbf{w} = \mathbf{0}, \\ & && \mathbf{c} \geq \mathbf{0}, \end{aligned}$$

which gives us Equation (4.4). The dual problem (4.5) corresponding to the upper endpoint $\bar{\theta}$ follows from an analogous derivation.

Appendix C. Simplification with full column rank and no constraints. We prove in this section that when $\text{rank}(\mathbf{K}) = p$ and there are no external constraints on \mathbf{x} , the solutions of problems (4.1) and (4.3) yield the interval $[\hat{\theta}_{\text{LS}} - z_{1-\alpha/2} \text{se}(\hat{\theta}_{\text{LS}}), \hat{\theta}_{\text{LS}} + z_{1-\alpha/2} \text{se}(\hat{\theta}_{\text{LS}})]$, where $\hat{\theta}_{\text{LS}} = \mathbf{h}^T \hat{\mathbf{x}}_{\text{LS}}$ is the plug-in estimator of θ , $\hat{\mathbf{x}}_{\text{LS}} = (\mathbf{K}^T \mathbf{K})^{-1} \mathbf{K}^T \mathbf{y}$ is the unregularized least-squares estimator of \mathbf{x} and $\text{se}(\hat{\theta}_{\text{LS}}) = \sqrt{\mathbf{h}^T (\mathbf{K}^T \mathbf{K})^{-1} \mathbf{h}}$ is the standard error of $\hat{\theta}_{\text{LS}}$.

Consider the lower endpoint of the interval. In the absence of external constraints on \mathbf{x} , the optimization problem (4.1) reduces to

$$(C.1) \quad \begin{aligned} & \text{minimize} && \mathbf{h}^T \mathbf{x} \\ & \text{subject to} && \|\mathbf{y} - \mathbf{K}\mathbf{x}\|^2 \leq z_{1-\alpha/2}^2 + s^2, \end{aligned}$$

where the slack factor s^2 is now defined as the objective function value of the corresponding unconstrained least-squares problem:

$$(C.2) \quad s^2 = \min_{\mathbf{x}} \|\mathbf{y} - \mathbf{K}\mathbf{x}\|^2.$$

Since we assume that \mathbf{K} has full column rank, the solution to the above problem is exactly $\hat{\mathbf{x}}_{\text{LS}} = (\mathbf{K}^T \mathbf{K})^{-1} \mathbf{K}^T \mathbf{y}$. Plugging in this value of $\hat{\mathbf{x}}_{\text{LS}}$, we obtain that the squared slack is given by the residual sum of squares

$$(C.3) \quad s^2 = \|\mathbf{y} - \mathbf{K}(\mathbf{K}^T \mathbf{K})^{-1} \mathbf{K}^T \mathbf{y}\|^2.$$

We can then write the constraint in problem (C.1) as follows:

$$(C.4) \quad \|\mathbf{y} - \mathbf{K}\mathbf{x}\|^2 \leq z_{1-\alpha/2}^2 + \|\mathbf{y} - \mathbf{K}(\mathbf{K}^T \mathbf{K})^{-1} \mathbf{K}^T \mathbf{y}\|^2.$$

We can further manipulate the difference

$$(C.5) \quad \begin{aligned} \|\mathbf{y} - \mathbf{K}\mathbf{x}\|^2 - \|\mathbf{y} - \mathbf{K}(\mathbf{K}^T \mathbf{K})^{-1} \mathbf{K}^T \mathbf{y}\|^2 &= \mathbf{x}^T \mathbf{K}^T \mathbf{K} \mathbf{x} - 2\mathbf{y}^T \mathbf{K} \mathbf{x} + \mathbf{y}^T \mathbf{K}(\mathbf{K}^T \mathbf{K})^{-1} \mathbf{K}^T \mathbf{y} \\ &= \|\mathbf{x} - \hat{\mathbf{x}}_{\text{LS}}\|_{\mathbf{K}^T \mathbf{K}}^2, \end{aligned}$$

where we have used the weighted-norm notation $\|\mathbf{x}\|_{\mathbf{A}} = \sqrt{\mathbf{x}^T \mathbf{A} \mathbf{x}}$, to arrive at the following program for the lower endpoint of the interval:

$$(C.6) \quad \begin{aligned} & \text{minimize} && \mathbf{h}^T \mathbf{x} \\ & \text{subject to} && \|\mathbf{x} - \hat{\mathbf{x}}_{\text{LS}}\|_{\mathbf{K}^T \mathbf{K}}^2 \leq z_{1-\alpha/2}^2. \end{aligned}$$

We proceed to show that the optimal value of this problem is given by $\hat{\theta}_{\text{LS}} - z_{1-\alpha/2} \text{se}(\hat{\theta}_{\text{LS}})$. We begin by writing down the Karush–Kuhn–Tucker (KKT) conditions [3] of the problem. The Lagrangian of the problem is given by

$$(C.7) \quad L(\mathbf{x}, \lambda) = \mathbf{h}^T \mathbf{x} + \lambda \left(\|\mathbf{x} - \hat{\mathbf{x}}_{\text{LS}}\|_{\mathbf{K}^T \mathbf{K}}^2 - z_{1-\alpha/2}^2 \right),$$

where $\lambda \geq 0$ is a dual variable. The KKT conditions for the primal and dual optimal pair $(\mathbf{x}^*, \lambda^*)$ are thus

$$(C.8) \quad \mathbf{h} = -2\lambda^* \mathbf{K}^T \mathbf{K} (\mathbf{x}^* - \hat{\mathbf{x}}_{\text{LS}}),$$

using first-order optimality with respect to \mathbf{x} , along with

$$(C.9) \quad \lambda^* \left(\|\mathbf{x}^* - \hat{\mathbf{x}}_{\text{LS}}\|_{\mathbf{K}^T \mathbf{K}}^2 - z_{1-\alpha/2}^2 \right) = 0$$

from the complementary slackness condition. We find that $\lambda^* = \frac{1}{2z_{1-\alpha/2}} \|\mathbf{h}\|_{(\mathbf{K}^T \mathbf{K})^{-1}} \geq 0$ and $\mathbf{x}^* = \hat{\mathbf{x}}_{\text{LS}} - \frac{z_{1-\alpha/2}}{\|\mathbf{h}\|_{(\mathbf{K}^T \mathbf{K})^{-1}}} (\mathbf{K}^T \mathbf{K})^{-1} \mathbf{h}$ satisfy the KKT conditions and therefore provide a primal-dual optimal pair. Substituting the value of \mathbf{x}^* into the objective, we arrive at the desired lower endpoint. The upper endpoint results from a similar argument.

Acknowledgments. We are grateful to Amy Braverman, Mike Gunson, Ryan Tibshirani, Sivaraman Balakrishnan, as well as the participants of the OCO-2 March 2019 Uncertainty Quantification Breakout Meeting, the Statistical and Applied Mathematical Sciences Institute Spatial X Working Group, and the Carnegie Mellon University Statistical Methods for the Physical Sciences Research Group for helpful discussions and feedback at various stages throughout this work.

REFERENCES

- [1] L. BIEGLER, G. BIROS, O. GHATTAS, M. HEINKENSCHLOSS, D. KEYES, B. MALLICK, Y. MARZOUK, L. TENORIO, B. VAN BLOEMEN WAANDERS, AND K. WILLCOX, *Large-Scale Inverse Problems and Quantification of Uncertainty*, John Wiley & Sons, 2011.
- [2] H. BOESCH ET AL., *Orbiting Carbon Observatory-2 & 3: Level 2 Full Physics Retrieval Algorithm Theoretical Basis*, NASA Jet Propulsion Laboratory, January 2, 2019. OCO D-55207, Version 2.0 Rev 3.
- [3] S. BOYD AND L. VANDENBERGHE, *Convex Optimization*, Cambridge University Press, 2004.
- [4] B. CONNOR ET AL., *Quantification of uncertainties in OCO-2 measurements of XCO₂: Simulations and linear error analysis*, *Atmospheric Measurement Techniques*, 9 (2016), pp. 5227–5238, <https://doi.org/10.5194/amt-9-5227-2016>.
- [5] B. J. CONNOR, H. BOESCH, G. TOON, B. SEN, C. MILLER, AND D. CRISP, *Orbiting Carbon Observatory: Inverse method and prospective error analysis*, *Journal of Geophysical Research: Atmospheres*, 113 (2008).
- [6] N. CRESSIE, *Mission CO₂ntrol: A statistical scientist’s role in remote sensing of atmospheric carbon dioxide*, *Journal of the American Statistical Association*, 113 (2018), pp. 152–168.
- [7] N. CRESSIE, R. WANG, M. SMYTH, AND C. E. MILLER, *Statistical bias and variance for the regularized inverse problem: Application to space-based atmospheric CO₂ retrievals*, *Journal of Geophysical Research: Atmospheres*, 121 (2016), pp. 5526–5537.
- [8] D. CRISP ET AL., *The Orbiting Carbon Observatory (OCO) mission*, *Advances in Space Research*, 34 (2004), pp. 700–709.
- [9] D. L. DONOHO, *Statistical estimation and optimal recovery*, *The Annals of Statistics*, 22 (1994), pp. 238–270.
- [10] A. ELDERING, C. W. O’DELL, P. O. WENNBERG, D. CRISP, M. GUNSON, C. VIATTE, C. AVIS, A. BRAVERMAN, ET AL., *The Orbiting Carbon Observatory-2: First 18 months of science data products*, *Atmospheric Measurement Techniques*, 10 (2017), pp. 549–563, <https://doi.org/10.5194/amt-10-549-2017>.
- [11] A. ELDERING, T. E. TAYLOR, C. W. O’DELL, AND R. PAVLICK, *The OCO-3 mission: Measurement objectives and expected performance based on 1 year of simulated data*, *Atmospheric Measurement Techniques*, 12 (2019), pp. 2341–2370.
- [12] A. ELDERING, P. WENNBERG, D. CRISP, D. SCHIMEL, M. GUNSON, A. CHATTERJEE, J. LIU, F. SCHWANDNER, Y. SUN, C. O’DELL, ET AL., *The Orbiting Carbon Observatory-2 early science investigations of regional carbon dioxide fluxes*, *Science*, 358 (2017), eaam5745.
- [13] H. W. ENGL, M. HANKE, AND A. NEUBAUER, *Regularization of Inverse Problems*, Kluwer, 2000.
- [14] P. C. HANSEN, *Rank-deficient and discrete ill-posed problems: Numerical aspects of linear inversion*, SIAM, 2005.
- [15] J. HOBBS, A. BRAVERMAN, N. CRESSIE, R. GRANAT, AND M. GUNSON, *Simulation-based uncertainty quantification for estimating atmospheric CO₂ from satellite data*, *SIAM/ASA Journal on Uncertainty*

- Quantification, 5 (2017), pp. 956–985.
- [16] J. HOBBS, M. KATZFUSS, D. ZILBER, J. BRYNJARSDÓTTIR, A. MONDAL, AND V. BERROCAL, *Spatial retrievals of atmospheric carbon dioxide from satellite observations*, 2020. In preparation.
- [17] A. E. HOERL AND R. W. KENNARD, *Ridge regression: Biased estimation for nonorthogonal problems*, *Technometrics*, 12 (1970), pp. 55–67.
- [18] T. ISAAC, N. PETRA, G. STADLER, AND O. GHATTAS, *Scalable and efficient algorithms for the propagation of uncertainty from data through inference to prediction for large-scale problems, with application to flow of the Antarctic ice sheet*, *Journal of Computational Physics*, 296 (2015), pp. 348–368.
- [19] J. KAIPIO AND E. SOMERSALO, *Statistical and Computational Inverse Problems*, Springer, 2005.
- [20] M. KIEL, C. W. O’DELL, B. FISHER, A. ELDERING, R. NASSAR, C. G. MACDONALD, AND P. O. WENNERBERG, *How bias correction goes wrong: measurement of X_{CO_2} affected by erroneous surface pressure estimates*, *Atmospheric Measurement Techniques*, 12 (2019).
- [21] S. KULAWIK ET AL., *Consistent evaluation of ACOS-GOSAT, BESD-SCIAMACHY, CarbonTracker, and MACC through comparisons to TCCON*, *Atmospheric Measurement Techniques*, 9 (2016), pp. 683–709, <https://doi.org/10.5194/amt-9-683-2016>.
- [22] M. KUUSELA, *Uncertainty quantification in unfolding elementary particle spectra at the Large Hadron Collider*, PhD thesis, EPFL, 2016.
- [23] M. KUUSELA AND V. M. PANARETOS, *Statistical unfolding of elementary particle spectra: Empirical Bayes estimation and bias-corrected uncertainty quantification*, *The Annals of Applied Statistics*, 9 (2015), pp. 1671–1705.
- [24] M. KUUSELA AND P. B. STARK, *Shape-constrained uncertainty quantification in unfolding steeply falling elementary particle spectra*, *The Annals of Applied Statistics*, 11 (2017), pp. 1671–1710.
- [25] O. LAMMINPÄÄ, J. HOBBS, J. BRYNJARSDÓTTIR, M. LAINE, A. BRAVERMAN, H. LINDQVIST, AND J. TAMMINEN, *Accelerated MCMC for satellite-based measurements of atmospheric CO_2* , *Remote Sensing*, 11 (2019), <https://doi.org/10.3390/rs11172061>.
- [26] J. MARTIN, L. C. WILCOX, C. BURSTEDDE, AND O. GHATTAS, *A stochastic Newton MCMC method for large-scale statistical inverse problems with application to seismic inversion*, *SIAM Journal on Scientific Computing*, 34 (2012), pp. A1460–A1487, <https://doi.org/10.1137/110845598>.
- [27] K. P. MURPHY, *Machine Learning: A Probabilistic Perspective*, MIT Press, 2012.
- [28] H. NGUYEN, N. CRESSIE, AND J. HOBBS, *Sensitivity of optimal estimation satellite retrievals to misspecification of the prior mean and covariance, with application to OCO-2 retrievals*, *Remote Sensing*, 11 (2019), <https://doi.org/10.3390/rs11232770>.
- [29] C. W. O’DELL ET AL., *The ACOS CO_2 retrieval algorithm - Part 1: Description and validation against synthetic observations*, *Atmospheric Measurement Techniques*, 5 (2012), pp. 99–121, <https://doi.org/10.5194/amt-5-99-2012>.
- [30] C. W. O’DELL ET AL., *Improved retrievals of carbon dioxide from Orbiting Carbon Observatory-2 with the version 8 ACOS algorithm*, *Atmospheric Measurement Techniques*, 11 (2018), pp. 6539–6576, <https://doi.org/10.5194/amt-11-6539-2018>.
- [31] A. K. RAMANATHAN, H. M. NGUYEN, X. SUN, J. MAO, J. B. ABSHIRE, J. M. HOBBS, AND A. J. BRAVERMAN, *A singular value decomposition framework for retrievals with vertical distribution information from greenhouse gas column absorption spectroscopy measurements*, *Atmospheric Measurement Techniques*, 11 (2018), pp. 4909–4928.
- [32] P. J. RAYNER AND D. M. O’BRIEN, *The utility of remotely sensed CO_2 concentration data in surface source inversions*, *Geophysical Research Letters*, 28 (2001), pp. 175–178.
- [33] C. D. RODGERS, *Inverse Methods for Atmospheric Sounding: Theory and Practice*, World Scientific, 2000.
- [34] D. RUPPERT, M. P. WAND, AND R. J. CARROLL, *Semiparametric Regression*, Cambridge University Press, 2003.
- [35] B. W. RUST AND W. R. BURRUS, *Mathematical programming and the numerical solution of linear equations*, American Elsevier, 1972.
- [36] B. W. RUST AND D. P. O’LEARY, *Confidence intervals for discrete approximations to ill-posed problems*, *Journal of Computational and Graphical Statistics*, 3 (1994), pp. 67–96.
- [37] P. B. STARK, *Inference in infinite-dimensional inverse problems: Discretization and duality*, *Journal of Geophysical Research: Solid Earth*, 97 (1992), pp. 14055–14082.

- [38] P. B. STARK, *Simultaneous confidence intervals for linear estimates of linear functionals*, Tech. Report 417, University of California, Berkeley, 1995.
- [39] P. B. STARK, *Constraints versus priors*, SIAM/ASA Journal on Uncertainty Quantification, 3 (2015), pp. 586–598.
- [40] P. B. STARK AND L. TENORIO, *A primer of frequentist and Bayesian inference in inverse problems*, in Large-Scale Inverse Problems and Quantification of Uncertainty, L. Biegler, G. Biros, O. Ghattas, M. Heinkenschloss, D. Keyes, B. Mallick, Y. Marzouk, L. Tenorio, B. van Bloemen Waanders, and K. Willcox, eds., John Wiley & Sons, 2011, ch. 2, pp. 9–32.
- [41] M. L. STEIN, *Interpolation of Spatial Data: Some Theory for Kriging*, Springer, 1999.
- [42] A. M. STUART, *Inverse problems: A Bayesian perspective*, Acta Numerica, 19 (2010), pp. 451–559.
- [43] A. TARANTOLA, *Inverse Problem Theory and Methods for Model Parameter Estimation*, SIAM, 2005.
- [44] L. TENORIO, *An Introduction to Data Analysis and Uncertainty Quantification for Inverse Problems*, SIAM, 2017.
- [45] L. TENORIO, A. FLECK, AND K. MOSES, *Confidence intervals for linear discrete inverse problems with a non-negativity constraint*, Inverse Problems, 23 (2007), pp. 669–681.
- [46] D. VAN DYK, A. CONNORS, D. N. ESCH, P. FREEMAN, H. KANG, M. KAROVSKA, V. KASHYAP, A. SIEMIGINOWSKA, AND A. ZEAS, *Deconvolution in high-energy astrophysics: science, instrumentation, and methods*, Bayesian Analysis, 1 (2006), pp. 189–235, <https://doi.org/10.1214/06-BA107>.
- [47] L. WASSERMAN, *All of Statistics: A Concise Course in Statistical Inference*, Springer, 2004.
- [48] I. S. WEIR, *Fully Bayesian reconstructions from single-photon emission computed tomography data*, Journal of the American Statistical Association, 92 (1997), pp. 49–60, <https://doi.org/10.1080/01621459.1997.10473602>.
- [49] L. WU, O. HASEKAMP, H. HU, J. LANDGRAF, A. BUTZ, J. AAN DE BRUGH, I. ABEN, D. F. POLLARD, D. W. T. GRIFFITH, D. G. FEIST, D. KOSHELEV, F. HASE, G. C. TOON, H. OHYAMA, I. MORINO, J. NOTHOLT, K. SHIOMI, L. IRACI, M. SCHNEIDER, M. DE MAZIÈRE, R. SUSSMANN, R. KIVI, T. WARNEKE, T.-Y. GOO, AND Y. TÉ, *Carbon dioxide retrieval from OCO-2 satellite observations using the RemoTeC algorithm and validation with TCCON measurements*, Atmospheric Measurement Techniques, 11 (2018), pp. 3111–3130, <https://doi.org/10.5194/amt-11-3111-2018>.
- [50] D. WUNCH ET AL., *Comparisons of the Orbiting Carbon Observatory-2 (OCO-2) X_{CO2} measurements with TCCON*, Atmospheric Measurement Techniques, 10 (2017), pp. 2209–2238, <https://doi.org/10.5194/amt-10-2209-2017>.
- [51] B. ZHANG, N. CRESSIE, AND D. WUNCH, *Inference for errors-in-variables models in the presence of spatial and temporal dependence with an application to a satellite remote sensing campaign*, Technometrics, 61 (2019), pp. 187–201, <https://doi.org/10.1080/00401706.2018.1476268>.